UNIVERSITÀ DEGLI STUDI DI MILANO

FACOLTÀ DI SCIENZE E TECNOLOGIE

Dipartimento di Fisica "Aldo Pontremoli"

Corso di Laurea Triennale in Fisica

Monte Carlo Study of the MULTIPASS Detector for Range Monitoring in Hadrontherapy

Internal Advisor:
Prof. Ivan Veronese

External Advisor:
Dott.ssa Ilaria Mattei

Candidate:
Cecilia Gaiani
Student ID: 969330

Academic Year 2023-2024

Monte Carlo Study of the MULTIPASS Detector for Range Monitoring in Hadrontherapy

Cecilia Gaiani

Dipartimento di Fisica, Università degli Studi di Milano

Via Celoria 16, 20133 Milano, Italia

Abstract

Charged Particle Therapy (CPT) is currently a widely used therapeutic alternative which employs beams of charged hadrons (protons or carbon ions) for the treatment of solid tumors. A CPT treatment lasts approximately 4 weeks, delivering a total dose of around 60-70 Gy to the tumor in fractions of approximately 2 Gy (around 30-35 fractions). During the interaction of the incident radiation with the tumor, various types of secondary particles are produced, including charged fragments, neutrons, and prompt photons, which can be utilized for range monitoring. To date, only post-treatment monitoring using PET scanners is available: there are no detectors capable of monitoring the beam range during the treatment itself (online range monitoring), nor are there techniques for monitoring the range between different treatment fractions (inter-fractional range monitoring). This thesis work is part of the PRIN MULTIPASS (MULTIPle trAcker for Secondary particleS monitoring) project, which aims to develop, construct, and test a prototype of a compact scintillating fiber monitoring device capable of detecting secondary radiation produced during CPT treatments, namely secondary protons and prompt photons for inter-fractional range monitoring, and neutrons for their characterization in terms of emission direction and energy. In this thesis project, a preliminary study is presented, based on Monte Carlo simulations performed with the FLUKA code, of the flux of secondary particles (p, n, γ) expected to enter the detector, in treatments with protons or carbon ions. This information is necessary for the design of the MULTIPASS readout electronics, based on SPAD (Single Photon Avalanche Diodes) arrays.

Contents

Introduction

Malignant neoplasms, generally defined as tumors, are cellular masses that originate from the uncontrolled reproduction of genetically altered cells within the body. Unlike benign tumors, which are usually localized and non-invasive, malignant tumors tend to invade surrounding tissues and rapidly spread. They consist of less differentiated cells and are more likely to metastasize, meaning they can diffuse to other parts of the body and produce secondary lesions [1] [2].

As observed in the report "I numeri del cancro 2023" [3], there has been a rise in cancer incidence rates among both males and females. It is estimated that in 2023 there were 395,000 new cancer diagnoses, with around 208,000 among men, an increase of 3,000 cases compared to 2022, and around 187,000 among women, with an increase of 1,000 cases compared to 2022.

Furthermore, malignant tumors still have a very high mortality rate. According to the World Health Organization (WHO), cancer remains one of the leading causes of death worldwide [4]. Therefore, cancer control represents a current issue of significant interest.

The most common therapies for tumors today include:

- Surgical removal, mainly for solid and localized tumors;
- Chemotherapy, the administration of cytotoxic drugs which target rapidly dividing cells, making it particularly suitable for treating fast-growing tumors by slowing their development and halting progression;
- Immunotherapy, a range of treatments that aim to educate the patient's immune system to attack cancer cells, treating them similarly to pathogens;
- Radiotherapy, the use of ionizing radiations which, by depositing energy (quantified by dose) in the treatment area, damage the genetic material of cancer

cells, preventing their reproduction and leading to apoptosis (programmed cell death).

In radiotherapy, two main approaches are possible. The first is conventional radiotherapy, which uses photons, in an energy range of $5 \div 10$ MeV (X-rays), or electrons, in an energy range of $4 \div 25$ MeV. This is one of the most widely used techniques for treating various types of cancer, mainly because its effects on the body are well understood and survival rates are relatively high. The second is Charged Particle Therapy (CPT), also called hadrontherapy, which employs beams of heavy ions, mainly protons (in the energy range of $50 \div 250$ MeV) and ^{12}C ions (in the range of $60 \div 400$ MeV/u). Interest in hadrontherapy is growing due to its numerous advantages over conventional radiotherapy. The latter is not suitable for treating deep tumors located close to vital organs, which would be damaged by the dose deposited by photons. In contrast, the depth-dose profile of heavy ions is more advantageous. Heavy charged particles release most of their energy at the end of their path within the target area, in a narrow region called Bragg Peak, whose position depends on the initial energy of the beam. This means that, by adjusting the energy of the radiation used for the treatment, a precise dose delivery is possible, maximizing the energy released in the tumor region while sparing healthy surrounding tissues.

Currently, there are several challenges which limit the widespread use of hadrontherapy techniques. First, the production of secondary particles occurring when the primary beam releases energy, especially neutrons. The characterization of ultra-fast secondary neutrons is very complex. They travel long distances within the patient's body before being absorbed, and they are responsible for dose deposition far from the tumor. As a result, neutrons are one of the main causes of secondary neoplasms arising away from the primary cancer. This poses a serious problem, especially in patients with long life expectancy, such as pediatric ones.

Another unresolved issue concerns range monitoring. Changes in the patient's morphology along the primary beam's propagation path may cause the variation of the position of the Bragg Peak, leading to the underdosage of the tumor and the overdosage of healthy tissues. Therefore, it is essential to determine where dose is actually deposited during the treatment. This can be achieved by tracking secondary particles emitted during the therapy, as secondary protons and prompt

photons. Those with sufficient energy to exit the patient's body can be detected using appropriate detectors, and through reconstruction algorithms their emission position, which is related to the Bragg peak location, can be backtracked. If significant variations on secondary emission distribution are observed with respect to the expectation, the treatment plan is revised. However, no devices are currently available for online range monitoring (during the treatment) nor inter-fractional range monitoring (between different treatment sessions).

In this context, the MULTIPASS (MULTIPle trAcker for Secondary particleS monitoring) project has emerged as an innovative initiative under the PRIN (Progetti di Rilevante Interesse Nazionale) program. It aims to design, build, and test a new scintillating fiber detector, capable of detecting multiple types of secondary particles, including both protons and prompt photons for inter-fractional range monitoring, and neutrons for their characterization in terms of energy and emission direction. The project is ambitious, since no detectors with such performance exist today. The crucial part of the MULTIPASS project is the design of the read-out electronics, based on Single Photon Avalanche Diodes (SPAD) technology. It will be developed in collaboration with Centro Ricerche "Enrico Fermi" (CREF, Roma) and Fondazione Bruno Kessler (FBK, Trento).

In this thesis work, a preliminary study was conducted using Monte Carlo simulations, performed with the FLUKA (FLUktuierende KAskade) code, to estimate the expected flux of secondary particles entering the detector, in order to drive the design of the electronics characteristics.

In the first part of the study, simulations were performed using a target made of a radiological tissue equivalent material, to assess the expected flux of secondary particles at production and entering the MULTIPASS detector in a simplified geometry, with secondaries produced by a single monoenergetic pencil beam of protons and carbon ions.

In the second part of the work, the CT (Computed Tomography) of two patients of the CNAO (Centro Nazionale di Adroterapia Oncologica) therapy center (Pavia), treated during a clinical trial, one with protons and the other with carbon ions, were used as simulation inputs, to assess the expected flux of secondary particles on the MULTIPASS detector in a real therapeutic scenario. The treatment plan of specific irradiation fields were included in these simulations.

The data obtained in the whole study are of great importance, since they will be used to optimize the development of the detector's read-out electronics, to ensure high performance in terms of detection accuracy and reconstruction precision.

Chapter 1

Charged Particle Therapy

This chapter defines the characteristics of the interaction between charged particles and matter, the biological effects of radiation, and how these effects can be exploited for therapeutic purposes.

1.1 Charged Particle Interactions with Matter

Charged particles interact with matter mainly through Coulomb interactions. The model that describes the loss of energy of charged particles in a material medium is known as Continuous Slowing Down Approximation (CSDA) [5]: the particle interacts with almost every atom along its path, losing only a small amount of its kinetic energy in each interaction. As a result, the deceleration and the energy loss can be treated as continuous phenomena. Four main types of interactions can occur, depending on the magnitude of the classical parameter of impact b of the incoming particle trajectory, compared to the measure of the atomic radius r_{atom} of the target atom, as shown in Figure 1.1:

- Inelastic hard (or close) collision: in this case, $b \approx r_{atom}$. The incident particle interacts with a single atomic electron, usually from an inner shell, causing its emission at high kinetic energy, resulting in δ rays (or knock-on electrons). This interaction is rare, but energy transfers are relatively large, so that the particle loses about 50% of its initial kinetic energy through hard collisions;
- Inelastic soft (or distant) collision: in this case, $b > r_{atom}$. The incoming particle interacts with the atom as a whole, exciting it and causing the emission

of a valence-shell electron. Even if the energy transferred to the absorbing medium in each interaction is quite small, soft interactions are more likely to occur. They account for half of the energy which is transferred to the medium;

- Inelastic radiative interaction: in this case $b < r_{atom}$. The incoming particle interacts with the atomic nucleus. This causes large energy losses, accompanied by the emission of Bremsstrahlung radiation;

- Elastic interaction: again, in this case, $b < r_{atom}$, and the incoming particle interacts with the atomic nucleus. However, no energy loss occurs. The direction of the incoming particle is only deviated from its original trajectory.

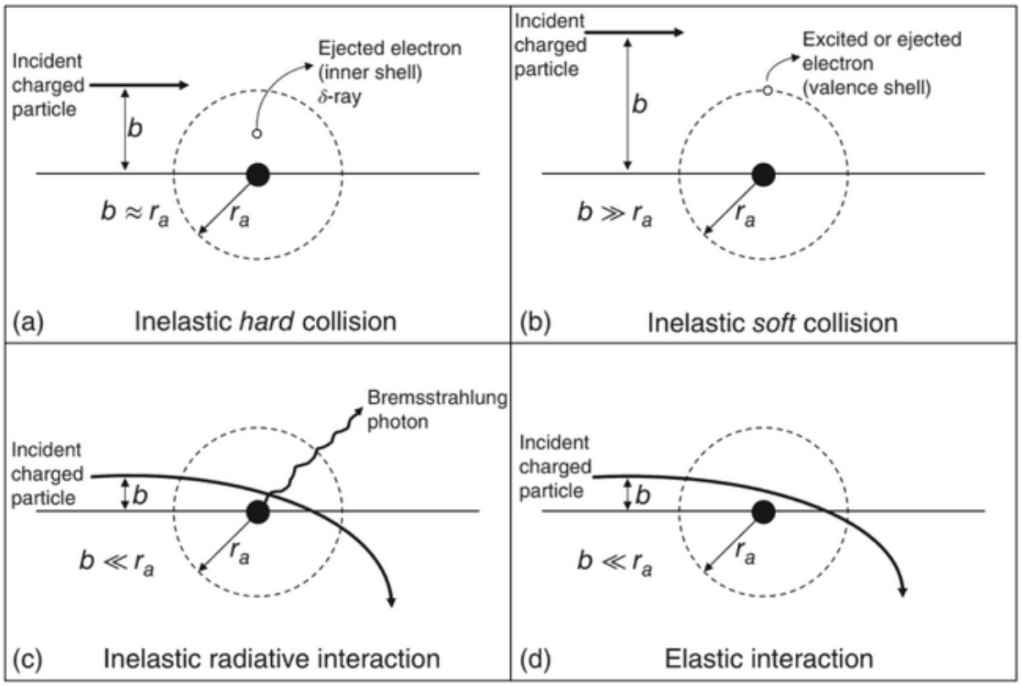

Figure 1.1: Representation of the interaction processes between charged particles and matter [6].

The quantity that defines the energy lost by a charged particle per unit of path length is known as Linear Stopping Power S, measured in MeV/mm or similar:

$$S = -\frac{dE}{dx} \ . \tag{1.1}$$

The total stopping power can be expressed as the sum of four components, which reflect the four energy transfer modes delineated just before, namely electronic stop-

ping power S_{el}, subdivided into a hard component S_{el}^{hard} and a soft component S_{el}^{soft}, radiative stopping power S_{rad} and nuclear stopping power S_{nucl}:

$$S = S_{el}^{hard} + S_{el}^{soft} + S_{rad} + S_{nucl} \ . \tag{1.2}$$

Focusing on heavy charged particles, such as protons and carbon ions, the stopping power analytic form was first estimated by Niels Bohr in 1913, using a classical approach, and later revised by Hans Albrecht Bethe and Felix Bloch in 1931 [7], including relativistic and quantum corrections. Bethe-Bloch's theory is based on the following assumptions:

- The charged particle moves so fast that atomic electrons can be considered stationary ($v_e \sim 0$, where v_e is the electron velocity);
- The incoming particle is much heavier than the orbital electrons ($m_p >> m_e$, where m_p and m_e are the particle mass and the electron mass, respectively);
- Only electromagnetic interactions with the target atom have to be considered, while nuclear reactions are negligible;
- The energy loss caused by the interaction with the atomic nucleus is negligible, so that $S \approx S_{el}^{soft} + S_{el}^{hard}$.

The Bethe-Bloch formula is the following [7]:

$$-\frac{dE}{dx} = 4\pi N_A r_e^2 m_e c^2 \rho \frac{Z_p^2}{\beta^2} \frac{Z_t}{A_t} \left[\frac{1}{2} \ln \left(\frac{2 m_e c^2 \beta^2 \gamma^2 T_{max}}{I^2} \right) - \beta^2 \right] \ , \tag{1.3}$$

where:

- N_A is the Avogadro number;
- r_e and m_e are the radius and the mass of the electron, respectively;
- ρ, Z_t and A_t are the density, the atomic number and the atomic mass of the target, respectively;
- Z_p and $\beta = v_p/c$ are the the mean atomic number and the velocity of the incident particle (divided by the speed of light c), respectively;

- T_{max} and I are the maximum kinetic energy that the impinging particle can transfer in a single interaction and the mean excitation/ionization potential of the target atomic electrons, namely the energy that the target absorbs from the projectile through ionization, respectively;
- $\gamma = (1 - \beta^2)^{-\frac{1}{2}}$ is the Lorentz factor.

Formula 1.3 is suitable for $0.1 \leq \beta\gamma \leq 1000$, which includes the energy range of particle therapy. However, at very low and very high energy, correction terms need to be applied:

- δ is the density correction term, relevant only for ultra-relativistic particles ($\beta\gamma > 1000$). It takes into account the effect of electronic polarization, which shields the Coulomb force field experienced by more distant electrons, thus reducing stopping power;
- C is the shell correction term, relevant only at very low energy ($\beta\gamma < 0.1$). Atomic electrons cease to participate to energy transfer when their velocity results comparable to that of the projectile particle. Ignoring this effect causes an overestimation of both I and Z_t, resulting in an underestimation of the stopping power. C is introduced to take account of this phenomenon.

The resulting formula is [7]:

$$-\frac{dE}{dx} = 4\pi N_A r_e^2 m_e c^2 \rho \frac{Z_p^2}{\beta^2} \frac{Z_t}{A_t} \left[\frac{1}{2} \ln \left(\frac{2m_e c^2 \beta^2 \gamma^2 T_{max}}{I^2} \right) - \beta^2 - \frac{\delta}{2} - \frac{C}{Z_t} \right] . \quad (1.4)$$

Considering the dependence on the incoming particle energy, four main regions are discernible, as shown in gray in Figure 1.2, which represents the stopping power as a function of the kinetic energy of antimuons impinging on a copper target. At low kinetic energies, the stopping power increases with the kinetic energy, until it reaches a peak at about $250I$. In this regions, shell corrections are very important. In the intermediate region, the stopping power decreases as $1/v^2$, reaching a broad minimum at 2-2.5 times the rest mass of the particle. In fact, raising velocity, the interaction time between the incoming particle and atomic electrons is reduced. So, the energy transferred to the medium is smaller, and the stopping power diminishes. In the region beyond the minimum, the stopping power increases with energy,

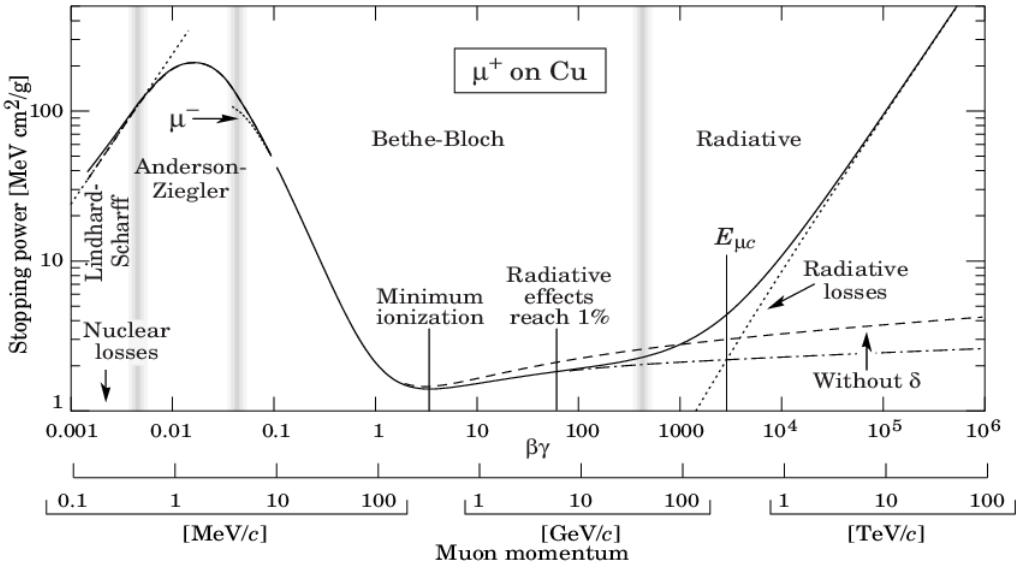

Figure 1.2: Trend of energy loss (stopping power) as a function of the energy of the incoming particle (here, antimuon on a copper target) [8].

because of the relativistic terms. At the beginning the rise is slow, while then is more marked. Also, radiative effects become appreciable. Moreover, it is evident an explicit dependence on the particle charge Z_p and velocity (through the β factor), but not from the mass of the projectile. Hence, an absorbing medium will have the same stopping power for all heavy charged particles with certain velocity and charge.

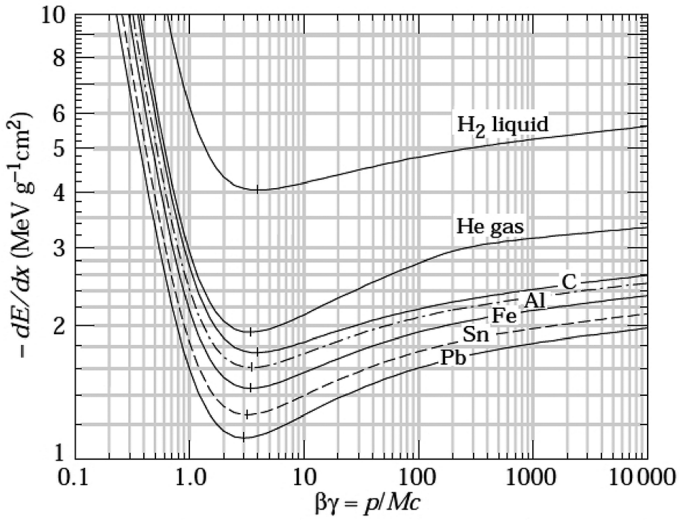

Figure 1.3: Stopping power, normalized on the density of the target, as a function of the energy of the incident particle (here, muons) for different target materials [8].

Instead, considering the dependence on the absorbing medium in the Bethe-Bloch formula, it is possible to notice the presence of three different terms:

- The ratio Z_t/A_t, which varies between 0.5 for low Z elements, and 0.4 for high Z elements, except for hydrogen, for which the value is 1: so, as Z_t/A_t increases, S decreases, as shown in Figure 1.3;
- The mean excitation/ionization potential I, which is the main factor contributing to the dependence on the absorbing medium. It grows with the atomic number of the target;
- The medium density ρ.

1.1.1 Bragg Peak (BP)

By observing Figure 1.2, it is evident that, for heavy charged particles, the majority of the energy is deposited when the velocity of the particle is low, or rather, at the end of its path, while energy deposition at the beginning of the crossed material is almost negligible.

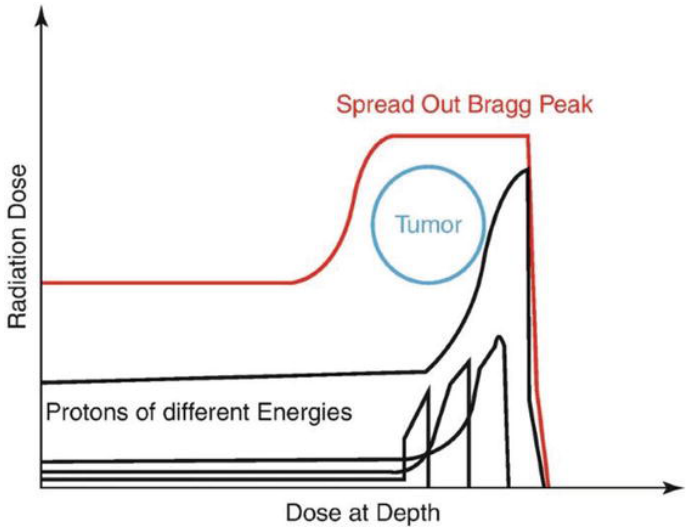

Figure 1.4: Superimposition of different primary proton beams at different energies to obtain the SOBP [9].

This characteristic peak is known as Bragg Peak (BP). The position of the Bragg peak depends on the energy of the particle beam: the higher is the energy, the deeper the Bragg peak is located. This feature is largely exploited, for example,

in Charged Particle Therapy (CPT) to irradiate deep tumors, since it allows to accurately radiate the sick region, sparing healthy tissues. Since the BP has a typical depth of the order of millimeters, to deliver a uniform dose to the entire tumor volume, many beams of different energies are superimposed, building the so called Spread Out Bragg Peak (SOBP), as shown in Figure 1.4.

1.1.2 Range

The range of a particle beam of determined energy and type, which travels in a specific material, is the expectation value of the path length that it follows in matter before it stops. Energy loss is intrinsically a statistical phenomenon, so a different amount of energy can be transferred to the medium in each interaction. The result is a statistical fluctuation in the range values of the particles of the beam, known as range straggling, which is of Gaussian type. Therefore, it is usual to refer to an average range, which can be determined experimentally by measuring the thicknesses of material that a monoenergetic and collimated particle beam impinging on it can penetrate.

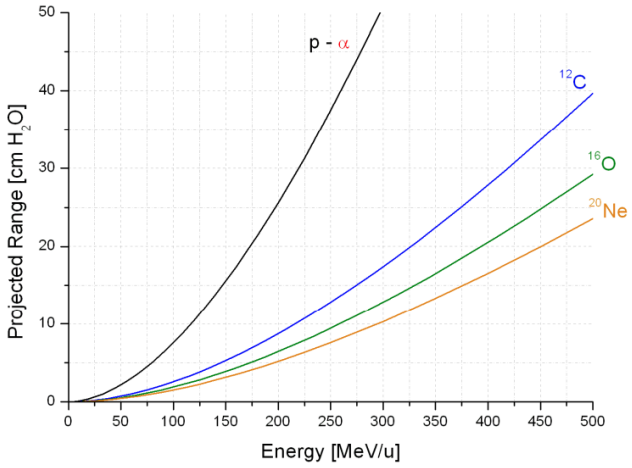

Figure 1.5: Range of different particles in water as a function of the kinetic energy of the incident particle [10].

Also, theoretical models can be handled. Indeed, it is possible to define the Continuous Slowing Down (CSDA) range for a particle of initial energy E_0:

$$R_{CSDA} = \int_0^{E_0} \left(\frac{dE'}{dx}\right)^{-1} dE' \ . \tag{1.5}$$

It is a calculated quantity that defines the distance travelled along the particle's trajectory, and not necessarily the depth of penetration. So, it is a good approximation of the average range of heavy charged particles, since their path in the absorbing medium is approximately rectilinear. Figure 1.5 shows the range as a function of the kinetic energy of the impinging particle for different projectiles.

1.1.3 Multiple Coulomb Scattering

In addition to range straggling, which occurs along the particle's track, elastic Coulomb scatterings between the projectiles and the atomic electrons cause a deflection of the trajectory in the target medium. The cumulative effect is a lateral spread of the impinging particle beam. For small angles and thin materials, the distribution of angular deflections is a Gaussian centered in $\theta = 0$ and of RMS θ_0, described by the Highland equation [11]:

$$f(\theta) = \frac{1}{\sqrt{2\pi\theta_0}} \exp\left\{\left(-\frac{\theta^2}{2\theta_0^2}\right)\right\} \ , \tag{1.6}$$

where:

$$\theta_0 = \frac{14.1\text{MeV}}{\beta cp} Z_p \sqrt{\frac{L}{L_0}} \left(1 + 0.0083 \ln\left(\frac{L}{L_0}\right)\right) \ , \tag{1.7}$$

and:

$$L_0 = 716.4 \ g \cdot cm^{-2} \frac{A_t}{Z_t(Z_t+1)\ln\left(\frac{287}{\sqrt{Z_t}}\right)} \ , \tag{1.8}$$

where A_t, Z_t and Z_p are, respectively, the mass number of the target, the atomic number of the target and the atomic number of the projectile; β and p are, respectively, the velocity of the impinging particle (divided by the speed of light c) and its momentum; L is the distance travelled by the particles in matter and L_0 is the radiation length of the absorbing material, a quantity related to the energy loss in it because of electromagnetic interactions. As perceivable by Equations 1.7 and 1.8, even if a larger Z_p causes a major beam broadening, the dependence on β and p

makes this effect more relevant in proton therapy, rather than in ^{12}C treatments. This approximation fails at large angles, where nuclear interactions may cause large angular deviations. A full description is provided by the Moliére theory [12].

1.1.4 Nuclear Fragmentation

In hadrontherapy, each primary beam particle has an energy up to hundreds of MeV/u, allowing nuclear interactions to take place. Two main processes might occur [7]:

- Elastic interactions: the kinetic energy of the impinging particle is conserved and the final effect is a lateral spread of the primary particle beam. They can occur at any energy;
- Inelastic interactions: provided that an appropriate threshold energy is exceeded, target nuclei and/or the impinging particle break, leading to the production of new particles. It is a many body problem, description of which is provided by the Quantum Chromodynamics (QCD) theory. However, at the energy of interest in CPT, only a perturbative approach can be managed.

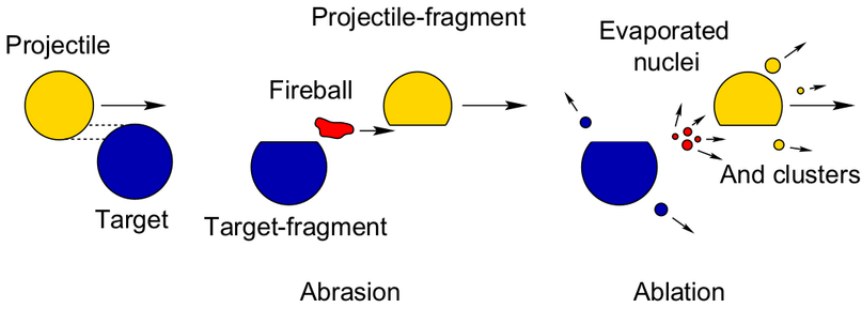

Figure 1.6: Illustration of the abrasion-ablation model [13].

Nuclear inelastic interactions are usually described by semi-empirical models. Both central or peripheral interactions can occur, according to the dimension of the impact parameter b. For small b, central collisions take place: in this case, all the nucleons of the nuclei are involved, causing the fragmentation of both the target and the projectile. In this case, light fragments with a very wide angular distribution can be produced. For large b, peripheral collisions happen. In this case, the nuclei overlap in a small region, resulting in the production of a few fragments

at approximately the same energy and incoming direction as the primary beam. Nuclear interactions are commonly described as a two stage process, as illustrated in Figure 1.6:

- Abrasion state: in this phase, the projectile interacts with the target nuclei, producing a highly reactive hot zone (fireball). The result is the formation of an excited pre-fragmentation structure, emitted at almost the same initial velocity, direction and ratio of mass over nuclear charge of the incident particle ($(A/Z)_f \sim (A/Z)_i$);
- Ablation state: it consists in the de-excitation of the excited fragments, mainly because of nuclear evaporation, leading to the production of γ-rays, protons, neutrons and light fragments with a kinetic energy of few MeV/u.

Even if it is a relatively unlikely process, it has to be considered in hadrontherapy, since fragments release energy in the patient's body, changing the total dose distribution.

1.2 Biological Effects of Radiation

1.2.1 Biological Damages

When ionizing radiation interacts with a biological target, it can cause DNA damage. Although this effect is particularly harmful to healthy tissues, it is extensively leveraged in clinical settings for cancer treatment, as already noted in Section 1.1.1. Actually, DNA damage is very common. Daily, the DNA of a single cell undergoes approximately 70,000 instances of damage [14], which can be classified into four types, presented in increasing order of severity and decreasing order of repairability [14]:

- Base damage: it is a common type of damage that involves the chemical modification of a single nucleotide. Approximately 25% of spontaneous lesions are of this type;
- Single Strand Break (SSB): it occurs when one of the two helices of the DNA is damaged. They account 75% of total daily lesions;

- Double Strand Break (DSB): it occurs when two SSB damage the same DNA molecule, resulting in a more severe lesion. It is estimated that there are about 25 cases out of the daily 70,000;

- Clustered lesions: they are complex lesions caused by the presence of two or more damaged sites within $10-20$ base pairs. They occur rarely spontaneously, are usually induced by radiation, and are difficult to repair.

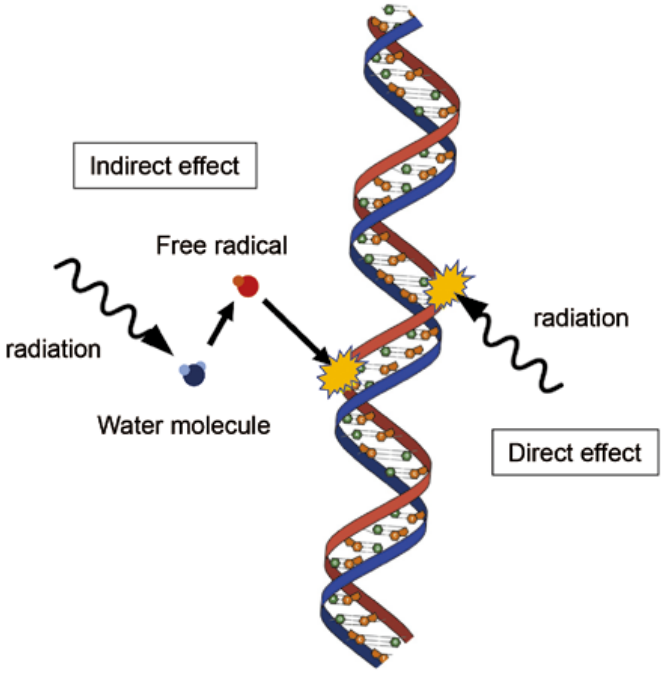

Figure 1.7: Representation of the mechanisms of direct and indirect DNA damage by ionizing radiation [15].

The goal of CPT is to inflict permanent damage to tumor tissues by inducing clustered lesions. DNA molecules can be damaged in two ways, as shown in Figure 1.7:

- Directly: radiation directly damages the DNA molecule;

- Indirectly: radiation ionizes water or oxygen molecules within the cell, leading to the formation of free radicals OH^*, which subsequently damage the DNA.

1.2.2 Dose

To quantify energy losses in biological tissues, a quantity known as dose D is used. It is defined as the energy absorbed for unit of mass, and it is measured in Gray (1 Gy = 1 J/kg):

$$D = \frac{dE}{dm} \ . \tag{1.9}$$

1.2.3 Linear Energy Transfer (LET)

The Linear Energy Transfer (LET) is the amount of energy dE that is locally transferred by ionizing radiation to the medium it traverses per unit length dl:

$$LET = \left(\frac{dE}{dl}\right)_{\Delta} \ , \tag{1.10}$$

where Δ is an upper threshold energy that indicates that only secondary electrons with energy less than Δ, which release energy close to the incident particle track, need to be considered, while those with higher energy will deposit energy elsewhere. Therefore, the LET takes into account the energy deposited in the vicinity of the particle track, by means of secondary electrons, and can be expressed as the energy lost in collisional events minus the kinetic energy of secondary electrons with energy greater than Δ. It is generally measured in keV/µm or similar.

The severity of the damage caused by ionizing radiation in cells is closely related to the LET. Photons, protons and electrons at clinical energies are low-LET radiations, ranging values from 0.2 keV/µm to 2 keV/µm. They release their energy in small, isolated ionizations, which are easily repaired by nuclear enzymes. Therefore, they are less effective in causing biological permanent damage. In contrast, carbon ions are a high-LET radiation. At therapeutic energies, their LET values range from 50 to 200 keV/µm. In this case, the LET and the ionization density change along the particle's path through the target, reaching their maximum at the Bragg peak. As a consequence, the damage inflicted on the cells is generally irreparable, leading them to death.

1.2.4 Relative Biological Effectiveness (RBE)

To account for the effect that different types of radiation have on various types of targets, a parameter called Relative Biological Effectiveness (RBE) was introduced. It is defined as the ratio between a reference dose D_{ref} (typically X-rays produced by 250 kV_p or γ rays emitted by the radioactive decay of ^{60}C) and the dose of interested radiation D_{test} that produces the same biological effect (isoeffect):

$$RBE = \frac{D_{ref}}{D_{test}}\bigg|_{iso} . \tag{1.11}$$

RBE depends on several factors, such as the incident radiation type, the biological effect used to define the isoeffect, and the type and condition of the target cells. Generally, to define D_{test}, the dose required to ensure that 10% of the diseased cells survive the irradiation is used.

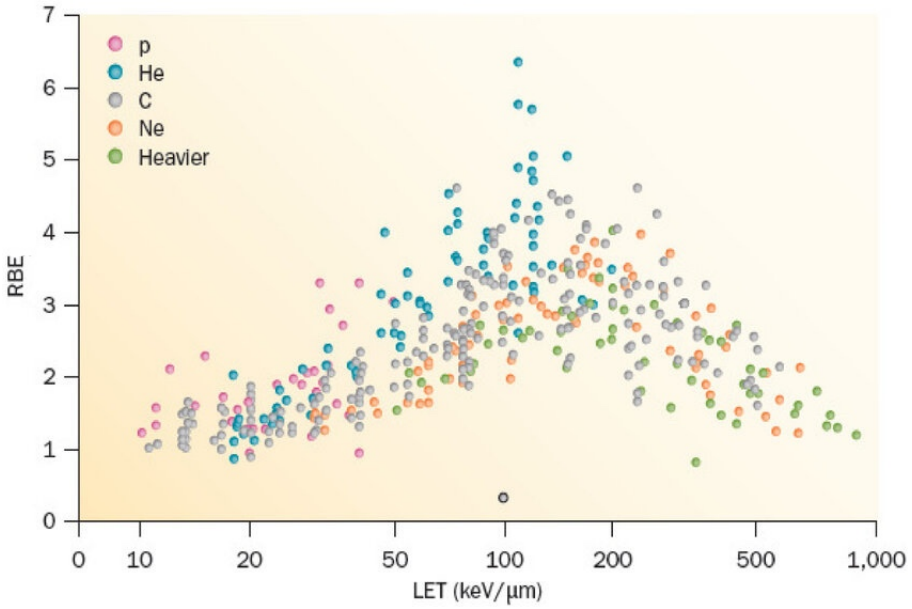

Figure 1.8: RBE trend as function of the LET for different particle types [16].

RBE is closely related to LET. As shown in Figure 1.8, RBE increases with LET until it reaches an optimal value (which depends on the ion considered), after which it decreases. In fact, high-LET particles have a high ionization density and are more likely to produce clustered damage, enhancing the effectiveness of the treatment. However, if a radiation with LET above the optimal value is used, additional lesions will be created where the DNA is already damaged, thereby reducing the biological

effect. This is known as overkill effect.

RBE is one of the most important factors to consider in treatment planning, as it is related to the biological dose D_{bio}, which reflects the potential biological damage of the radiation in question, and to the physical dose D_{phys}, which is the absorbed dose defined in Section 1.2.2, through the following equation:

$$D_{bio} = RBE \cdot D_{phys} \ , \tag{1.12}$$

The biological dose D_{bio}, is expressed in Gray Equivalent (GyE), which is the Gray (defined in Section 1.2.2) multiplied by the RBE. Quantifying the RBE thus allows medical physicists to understand the total physical dose D_{phys} that needs to be administered to the tumor.

1.2.5 Oxygen Enhancement Ratio (OER)

As mentioned in Section 1.2.1, the presence of free radicals in tissues significantly enhances the mechanism of indirect damage. In particular, the effectiveness of a particle treatment depends strongly on the oxygenation of the tissues: it has been observed that oxygenated tissues are more radiosensitive, whereas hypoxic tissues are less responsive to radiation. To quantify these effects, the Oxygen Enhancement Ratio (OER) is used:

$$OER = \left. \frac{D_{hypo}}{D_{air}} \right|_{iso} . \tag{1.13}$$

It is defined as the ratio between the radiation dose in hypoxia condition (D_{hypo}) over the radiation dose in aerobic condition (D_{air}), for the same biological effect (isoeffect).

The OER is of significant importance for photons (OER ~ 3), as they are low LET particles. Therefore, oxygen concentration can strongly influence the lesions caused. In contrast, for heavy charged particles it is less relevant (OER ~ 1), because they damage cells predominantly through direct mechanisms. Their radiobiological effectiveness is therefore independent of the presence of oxygen in tissues.

1.3 Treatment Planning System (TPS)

Hadrontherapy exploits the profile of the Bragg peak to precisely irradiate the tumor region, sparing healthy tissues. This is achieved also in conventional radiotherapy with photons, using advanced techniques as IMRT (Intensity Modulated Radiation Therapy), but, regarding the protection of unaffected areas, this is less favourable with respect to hadrontherapy. As depicted in Figure 1.9, the depth-dose profile shows that photons tend to deposit a large portion of their energy upon entering the target, making them less suitable for the treatment of deep tumors. Furthermore, they also release dose in the surrounding regions of the tumor, limiting their use in treating neoplasms located near vital organs.

On the other side, as explained in Section 1.1.1, heavy charged particles deposit high dose at a grater depth, succeeding in harming mainly the sick area. Typically, the radiation profile of the SOBP is used to irradiate the tumor at its depth, along with modulators (either active or passive [14]) that expand the cross-sectional area of the beam. Since in hadrontherapy high dose releases on a restricted area are implied, it is important to conveniently plan the radiation treatment and to verify its suitability in the course of time, checking where energy is actually deposited (or, in other words, measuring the range of the primary beam, as will be thoroughly examined in Chapter 2).

The preparation of the treatment plan is a relatively complex process. First of all, a few days before the radiation treatment, the patient undergoes a CT and/or an MRI scan, so that it is possible to identify shape and position of the tumor. Imaging also provides the input for the Treatment Planning System (TPS), which is a computerized tool used to design a specific customized radiation protocol and also to predict its consequences on the interested area.

Starting from imaging inputs, the TPS defines some specific regions, as shown in Figure 1.10, according to ICRU Report 50 and Report 62 [18]:

- Gross Tumor Volume (GTV): it is the region containing the malignant growth;
- Clinical Target Volume (CTV): it is a safe margin, surrounding the GTV, containing sub-clinical microscopic disease or regions at risk, which need to be irradiated to be eliminated;

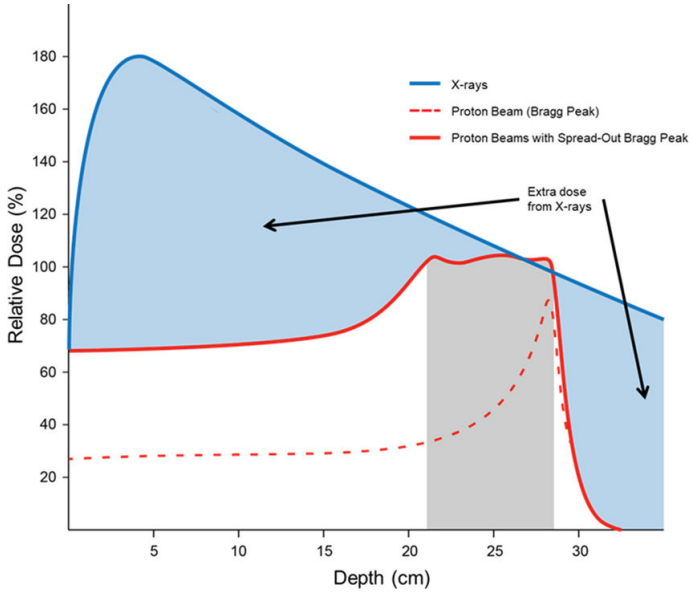

Figure 1.9: Comparison between the dose deposition of photons and protons. In gray, the tumor region [17].

- Internal Target Volume (ITV): it includes the CTV and an Internal Margin (IM), needed to take into account variations in size and position of the CTV;
- Planning Target Volume (PTV): it is a geometrical concept design to ensure that the prescribed dose is actually absorbed in the CTV. It is often described as the CTV plus a variable margin, named Safety Margin (SM), due to setup and instrument uncertainties. Generally, it is PTV $\sim$ CTV + 1 cm;
- Treated Volume (TV): it is the volume defined starting from an appropriate isodose curve (typically the 95% curve), chosen to ensure the effectiveness of the treatment plan;
- Irradiated Volume (IV): it is the region that receives a dose sufficient to affect healthy tissues;
- Organ at Risk (OAR): it is a healthy organ placed near the sick area, and sensitive to radiation. Its tolerance is significant considering the dose received from a treatment plan.

The TPS, when defining the safe margins and regions described above, takes into account range uncertainties sources, which are factors that may alter the range of the particles in the anatomical district. The aim is safeguarding healthy tissues and guaranteeing maximum efficiency of the treatment plan for tumor therapy.

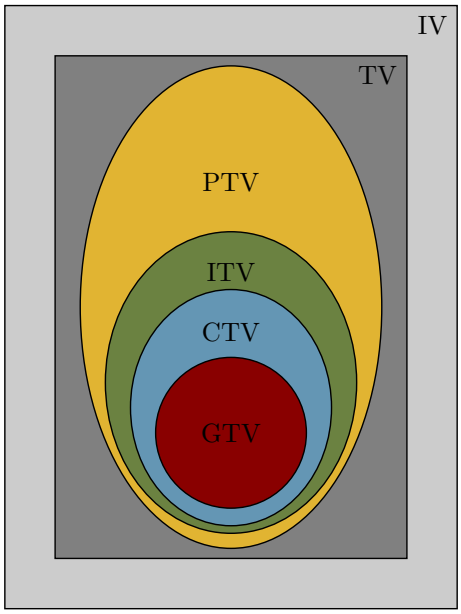

Figure 1.10: Anatomical regions defined by the TPS.

These factors include the finite resolution of the CT artefacts, the conversion of CT Hounsfield Units (HU) to tissue densities, density effects, due for example to the patient positioning or physiological organ motions (such as breathing), anatomical changes of the tumor recorded during the treatment, and the time that passes between the CT acquisition and the beginning of the therapy, or between a fraction and the other.

1.3.1 Target and Projectile Fragmentation

As mentioned in Section 1.1.4, following nuclear interactions between the target and the projectile, the phenomenon of fragmentation may occur. In the case of protons, only target fragmentation can occur. However, for projectiles with $A_p > 1$ (where A_p is the mass number of the projectile), fragmentation of the incident particles is also possible.

The heavy fragments produced by the projectile generally retain approximately the same velocity as the projectile, but with a lower mass, and are emitted at small angles relative to the direction of incidence. These fragments tend to release additional energy beyond the Bragg peak. On the other hand, the lighter fragments can be emitted at large angles, and release energy both beyond the Bragg peak and outside the prescribed dose region for energy deposition.

Furthermore, both in proton therapy and carbon ion therapy, target fragmentation can occur along the entire path of the particle through the medium, up to the Bragg peak. The produced fragments (mainly carbon, hydrogen, and oxygen) have a kinetic energy of at most a few MeV and a range of only a few µm, so they cannot escape the patient's body and be detected nor tracked. However, as they are absorbed by tissues, they can have a very high RBE.

1.4 Range Monitoring

To limit the contribution of the uncertainty sources mentioned in Section 1.3, it is necessary to make an opportune measurement of particles' range in matter. Different techniques can be carried out, and they are based on the detection of secondary particles produced in the interaction of the primary beam with the target. Usually, the particles used are [19]:

- Charged fragments: they are produced from the fragmentation of the primary beam particles (exclusively if the projectiles are ions with $Z_p > 1$) [20];
- Prompt-γs: the primary beam particles excite, through nuclear interactions, the target nuclei, which then decay ($\approx$ ns) emitting prompt photons with energies up to 10 MeV [21];
- PET-γs from $\beta+$ emitters: positrons emitted in $\beta+$ decays annihilate with stationary electrons, producing a back-to-back pair of photons at an angle of 180° and each having an energy of 511 keV. These photons can be detected by Positron Emission Tomography (PET) scanners [22];
- Neutrons: they are produced by nuclear interactions between the primary beam and the target [23] [24].

The beam range monitoring is possible thanks to the detection of the above listed particles. Two approaches are possible. The first is inter-fractional range monitoring, which consists in range detection between a fraction (treatment session) and the other, to verify whether morphological changes occurred, potentially requiring a change in the treatment plan. The second one is on-line range monitoring: the range is monitored during the treatment and, if significant dose distribution variations are

detected, the beam delivery is immediately interrupted. Range monitoring systems represent one of the main medical physics research topics nowadays, since they allow to significantly increase the effectiveness and the precision of hadrontherapy treatments.

1.4.1 Range Monitoring for Proton Treatments

In proton hadrontherapy, prompt-γ and PET-γ detection is exploited.

As explained in Section 1.4, $\beta+$ emitters monitoring is based on the detection of back-to-back photons emitted as consequence of the annihilation of positrons, emitted in $\beta+$ decays, with a stationary electron. The production of $\beta+$ radioactive isotopes can occur because of the nuclear interactions between the incident primary beam and the target, or target nuclear fragmentation (since protontherapy is treated in this Section, projectile fragmentation does not contribute).

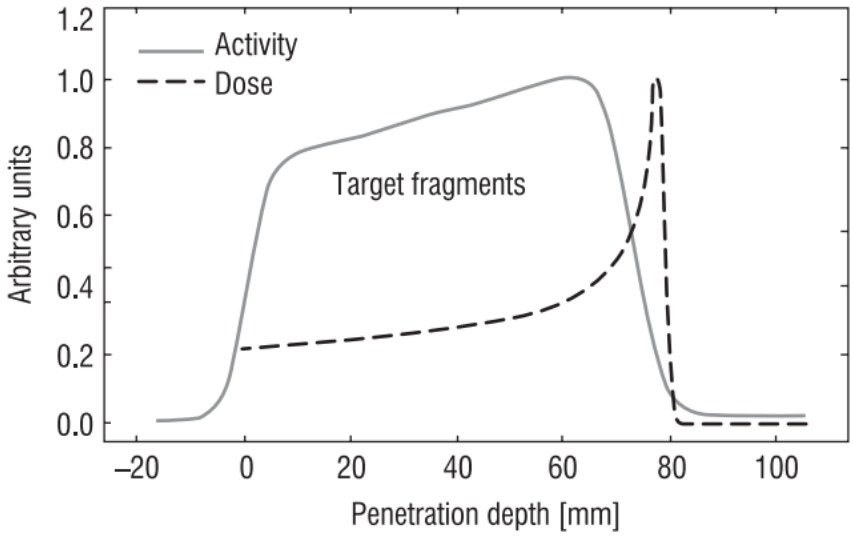

Figure 1.11: In-beam PET measurement of $\beta+$ activity and dose distribution as a function of the penetration depth for a PMMA target irradiated with 100 MeV protons [22].

As shown in Figure 1.11, the activity of $\beta+$ emitters is accentuated along the proton's path in the target. It rises, reaching a maximum, and then it rapidly disappears just before the Bragg peak. This property makes PET-γs suitable for range monitoring for proton hadrontherapy treatments, since they allow to conveniently

follow the energy deposition along the entire proton track, even if the correlation with the Bragg peak is more difficult to reconstruct.

Another important aspect to consider is the half life of the particular isotope chosen for monitoring: it must not be too long, in order to maximize the number of patients which can be treated each day.

PET-γ detection can be performed with three different techniques:

- Off-line monitoring: after the radiation treatment, the patient is moved to a different room, where PET-γ detection is performed [25] [26]. However, this technique faces the problem of metabolic wash-out, which consists in the expulsion from the human body of $\beta+$ emitters, recognized as foreign substances, by chemical reactions which occur in living tissues. Thus, while the patient is moved from a place to another, part of the radioactive isotopes used for detection are lost, causing a reduction of the correlation between the deposited dose and the metabolic activity. Moreover, it is a low-statistic procedure, so long times ($\sim$ 30 min) are necessary to collect enough data;

- In-room monitoring: PET-γ detection is performed in the same room of the radiation therapy [27]. Just after the treatment, the patient's bed is put in PET scanning position. This allows to reduce metabolic wash-out, but the overall treatment is longer, slowing down the clinical workflow;

- In-beam monitoring: the measurement of the $\beta+$ emitters activity is performed during the irradiation. This way, metabolic washout is avoided. However, this procedure is affected by huge background, since it is influenced by the presence of all particle types emitted during the treatment. Moreover, the arrangement of the necessary devices is generally difficult.

The other monitoring technique, that it is analyzed in this Section, is based on the detection of prompt-γs. The primary beam excites the target nuclei, which then decay to a stable state in typical times of about $10^{-16} \div 10^{-12}$ s, emitting prompt photons with energy of $1 \div 10$ MeV [28] [29]. Because of the fast emission, prompt-γs show a strong correlation with the Bragg peak, avoiding the problem of metabolic wash-out. Also, the extremely short decay time significantly accelerates the overall monitoring process. Moreover, prompt-γs emission is isotropic and each photon is

emitted independently from the others, differently from PET-γ detection, in which the detection of a couple of correlated photons is required. From the viewpoint of medical equipment, this means that for PET-γ monitoring a ring detector is required, while for prompt-γ monitoring a simpler device can be employed.

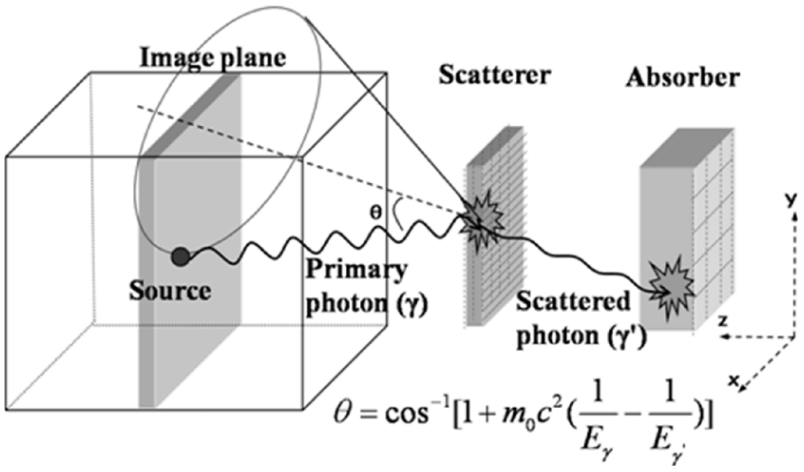

Figure 1.12: Functioning framework of a Compton camera [30].

The main disadvantages of this technique are the neutron component background, and the fact that, because of the wide energy spectrum, prompt-γs cannot be detected using standard techniques, since heavier and thicker absorbers are required, causing loss of efficiency and spatial resolution, in addition to weight limitations due to the bulk of the necessary medical equipment. Three main monitoring techniques for prompt-γ detection are performed:

- Imaging with passive collimators: this technique is based on the use of physical collimators (such as, multi slit, knife edge slit, or pinhole cameras), which have to be collocated between the patient and the detector, with the purpose of filtering background radiation and determining proton range with millimeter accuracy [21]. This system is actually implemented, but it is limited by low statistics and secondary neutron background;

- Imaging with active collimators: it is based on the use of Compton Cameras (CC) to reconstruct the position of emission of the photon in the detector,

exploiting Compton scattering [31]. A CC is made up of two parts: the scatter detector, where Compton scattering occurs, and the absorption detector, where the scattered photon is absorbed. As seen in Figure 1.12, from the measurement of the energy E_γ of the initial photon and of the energy $E_{\gamma'}$ of the scattered photon, it is possible to retrieve the scattering angle θ: the initial photon trajectory lies on a cone of angle θ;

- Non-imaging systems: they are based on the measurement of prompt-γs' Time Of Flight (TOF) or energy spectrum, to reconstruct the position of the Bragg peak.

1.4.2 Range Monitoring for ^{12}C Ions Treatments

In ^{12}C ion therapy (and, in general, if the treatment is delivered using ions with $Z_p > 1$), fragmentation of both target nuclei and primary particle projectile can occur, as explained in Section 1.3.1. This last one has a non-negligible cross section. It leads to the production of secondary charged particles, with lower Z compared to the initial one, which can be detected for range monitoring aims. Charged fragments produced in carbon ion treatments have velocities comparable to those of the primary beam, and kinetic energies up to 100 MeV. Therefore, once they leave the patient, it is easy to trace them. However, some of them do not have enough energy to leave the human body, causing a re-absorbtion phenomenon.

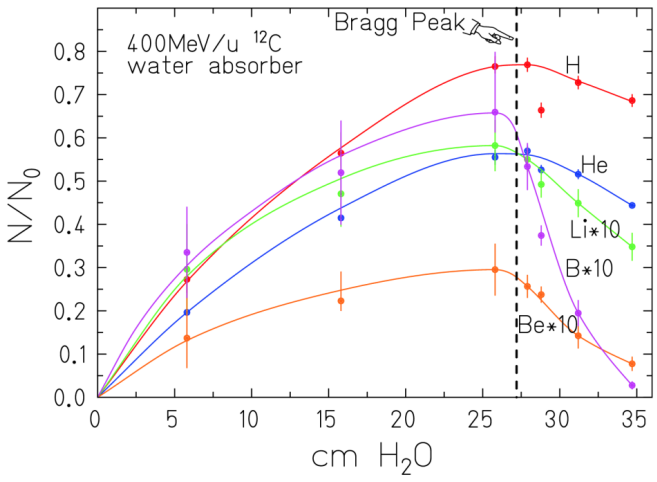

Figure 1.13: Fragments produced by 400 MeV/u ^{12}C ions in a water target as function of the penetration depth [32].

The majority of the fragments are produced in the forward direction, although a non-negligible fraction of them, mainly protons, is emitted at wider angles ($60° - 90°$). These particles can be easily detected and tracked, even if spatial resolution is affected by the MCS, described in Section 1.1.3. Figure 1.13 shows the fragments produced by a carbon beam at 400 MeV/u in water as a function of the penetration depth. It is observed that the production of charged secondaries increases with penetration depth, reaching a maximum at the Bragg peak. However, the fragments produced at the end of the beam's path have very low energy and are not useful for range monitoring, as they are reabsorbed by the patient's body and are not detectable at large angles, where detectors are positioned. For this reason, charged fragments generated at the entrance of the target are exploited.

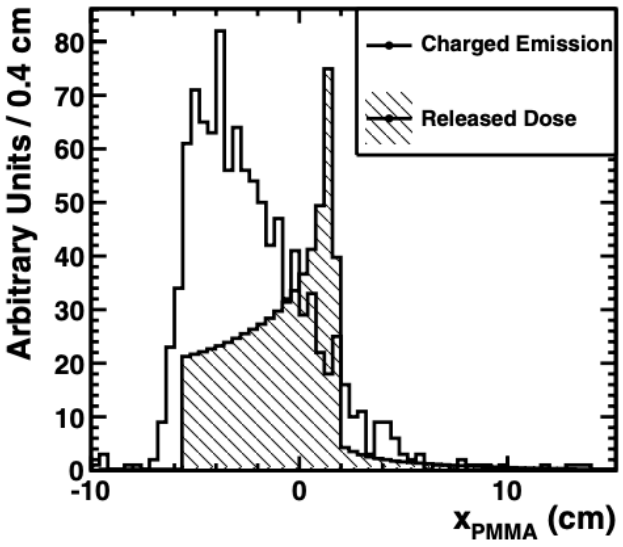

Figure 1.14: Production of secondary fragments detected at large angle and dose release as a function of the penetration depth in a PMMA target [33].

In Figure 1.14, it is shown the emission profile of secondary charged fragments production as function of penetration depth in a PMMA target. Superimposed, it is represented the dose release profile. It is evident that the two trends are anti-correlated [33]. Indeed, as previously outlined, the charged fragments produced in the entry region of the target possess a very high energy, enabling them to exit the treated area and to reach the detector. In contrast, those generated near the Bragg peak, although more abundant, have much lower energy and are typically reabsorbed by the patient's body. As a result, when reconstructing the emission profile of the

charged secondaries, the most significant contribution comes from those produced at the target's entry point, where dose deposition is lower.

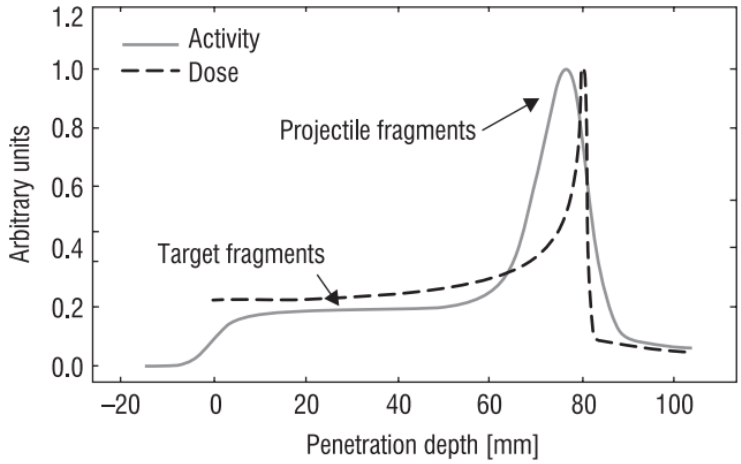

Figure 1.15: In-beam PET measurement of $\beta+$ activity and dose distribution in function of the penetration depth for a PMMA target irradiated with 212.12 MeV/u carbon ions [22].

With respect to proton treatments, PET-γ detection is not adequate for range monitoring in ^{12}C ions therapy. As shown in Figure 1.15, in the case of carbon treatments, $\beta+$ emitters are generated both from the fragmentation of the target and the projectile. Target fragments are emitted throughout the entire path of the primary beam within the target, resulting in a uniform low-activity profile. Conversely, projectile fragments are primarily produced nearby the Bragg peak. Indeed, at low energy, the projectile nuclear fragmentation cross-section is very high, leading to a significant production of charged secondaries at the Bragg peak, including $\beta+$ emitters. Because of the strict correlation with the Bragg peak, this activity peak in secondary fragments emission may be efficiently exploited to study the energy release in the Bragg peak. However, the main problem of this technique is the presence of high background due to secondary particles produced simultaneously to PET-γs.

In carbon ion treatments, it is possible to perform range monitoring based on prompt-γ detection, although the expected background statistics due to neutrons would be higher with respect to protontherapy.

Chapter 2

The MULTIPASS Project

This chapter presents the MULTIPASS research project, along with its corresponding objectives, in which this thesis work is contextualized, with particular attention to the approach followed.

2.1 Range Monitoring Limitations

Nowadays, beam range uncertainties are considered by specialists as the main obstacle to the effective spread of CPT treatments. In fact, the uncertainty in dose deposition accuracy makes it essential to properly define safety margins around the tumor, thereby delivering the maximal dose also to the healthy tissues surrounding the sick area. However, reducing the size of safety margins would be extremely important in the treatment of patients with long life expectancy, as pediatric ones, in order to avoid the development of secondary malignancies due to the high radiation exposure of healthy tissue. Moreover, it is of crucial importance in the case of tumours close to OARs, to avoid negatively impacting the patient's quality of life. Therefore, an accurate definition of particle range is necessary. Since it can be assessed through the detection of the particles described in Section 1.4, the accuracy in range measurement is closely related to the capability of detecting secondary radiation.

Another problem that must be considered is neutron radiation, which is emitted as a result of the interaction of the primary beam particles with biological tissues. Neutrons represent the most elusive component of secondary radiation. Indeed, since they do not interact electromagnetically with matter, they can travel long

distances within the patient before being stopped and absorbed. The consequence of this energy deposition away from the point of incidence of the beam is the potential development of secondary malignant neoplasms far from the primary tumor. Therefore, to optimize treatments, it is important to characterize neutron radiation in terms of both energy and emission angle.

The development of range monitoring techniques represents a significant challenge, but it is crucial, as it would advance hadrontherapy treatments significantly. Currently, only post-treatment monitoring using PET imaging is implemented, and only for a limited number of patients. Neither on-line nor inter-fractional monitoring is used in the medical workflow. Additionally, there is currently no available device that can characterize neutrons coming directly from the incident radiation, especially in terms of spatial emission distribution, while simultaneously detecting different particle types. In this context, the PRIN (Progetti di Rilevante Interesse Nazionale) MULTIPASS (MULTIPle trAcker for Secondary particleS monitoring) project is relevant. The aim of this project is to develop, construct, and test a prototype of a compact monitoring device capable of detecting secondary particles produced in CPT, specifically prompt-γ rays and protons, to verify morphological changes in tumor geometry between different therapeutic sessions (inter-fractional range monitoring, see Section 1.4), and to characterize the neutron radiation component.

2.1.1 The Detection of Charged Particles: the Dose Profiler

As reported in Section 1.4.2, the production of secondary charged particles, due to nuclear fragmentation, is significant when ^{12}C treatments are delivered. These fragments have, on average, a lower stopping power, and, as a consequence, their range is longer in comparison to the primary beam. Despite being a potentially damaging process, which has to be properly modeled by the TPS, the ambition is to exploit it for range monitoring. In particular, the on-line detection of high-energy proton radiation, which can pass through the patient's body and can be detected at large emission angles, with respect to the incoming beam direction, might be exploited. Fundamental data were acquired within the INSIDE (INnovative Solution for In-beam DosimEtry in hadrontherapy) project. Its aim is to develop an original technology to spot inter-fractional variations which the tumor might

undergo between the several treatment fractions, taking advantage of the emission profile of secondary charged particles. Actually, the INSIDE system is bimodal, i.e. it includes two PET scanners to detect PET photons in protontherapy, and a detector, named Dose Profiler (DP), to monitor charged fragments emitted in carbon ion therapies. A draft of the structure is depicted in Figure 2.1. DP is made up of 8 squared planes, each with a side of 19.2 cm and spaced 2 cm apart, composed of 500×500 μm^2 squared plastic scintillating fibers. At present, it is installed in treatment room n.1 of the CNAO (Centro Nazionale di Adroterapia Oncologica), in Pavia, at 50 cm from the room isocenter.

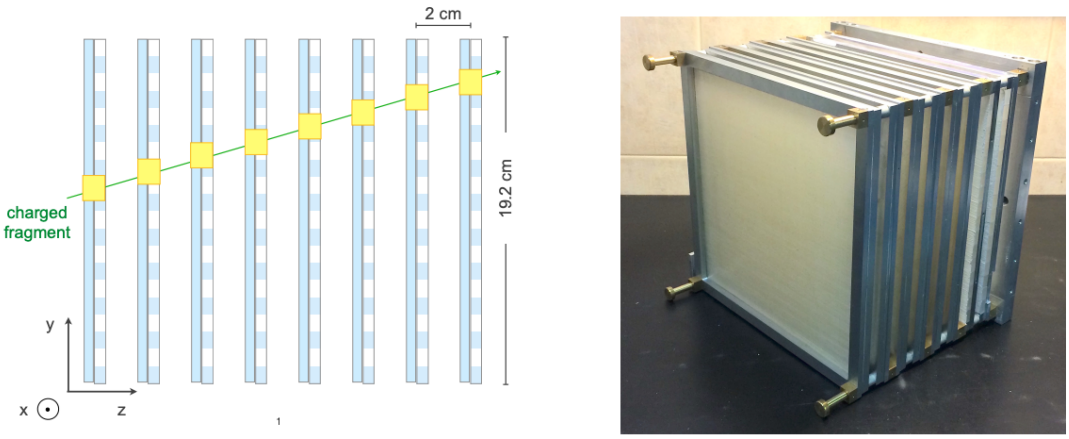

Figure 2.1: Left: Representation of the internal structure of DP. Superimposed in green, the trajectory of a charged particle entering the detector, while in yellow, the energy releases in the fiber planes. Right: DP during the assembly phase. In aluminium, the eight fiber planes. Figure from [34].

The first results, achieved during a clinical trial at the CNAO using DP, demonstrated the feasibility of such a detector, capable of identifying potential inhomogeneities in some of the treated patients [35]. However, the study also showed the limitations of DP. Firstly, the detector is collocated in a fixed position in space, far from the patient body. This reduces both the adaptability of the device, as it cannot be conformed to every possible patient bed configuration or tumor geometry, and the solid angle covered by the active surface. Secondly, it is quite bulky and heavy, which makes it difficult to handle and maintain. Moreover, it can sustain a rate of incidence of the order of 100 kHz, not enough to track the number of particles

originating from the regions where the majority of carbon ions is delivered.

MULTIPASS foresees to overcome the limits of DP. It is designed as a compact device which can be easily moved and positioned closer to the patient, satisfying any therapeutic request. The technological adjustments will also allow to increase the collectable statistic, and with the foreseen read-out electronics, the detector will sustain an impinging particle rate on the detecting volume of 500 kHz. Thanks to these expedients, the detector will conveniently be able to work as an inter-fractional monitoring system, capable of spotting anatomical changes in the course of the entire therapy.

2.1.2 The Detection of Prompt-γs: PAPRICA

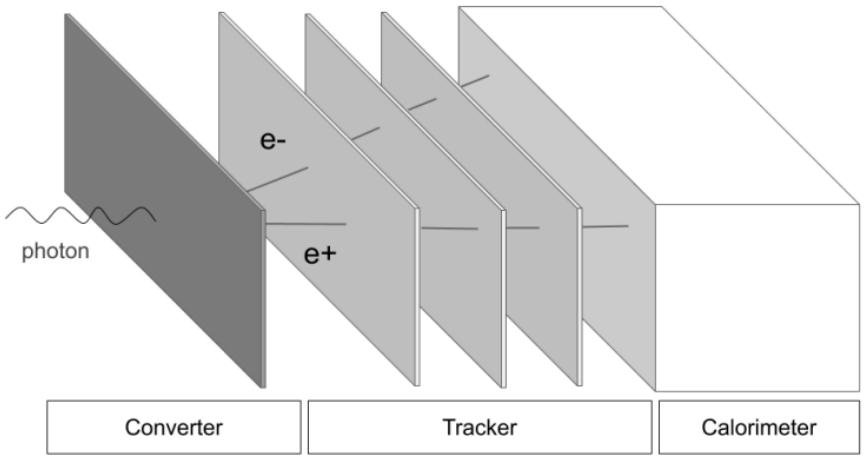

Figure 2.2: Schematic representation of the various parts of the PAPRICA detector. Note the converter, the tracker, and the calorimeter. Figure from [36].

The detection of prompt photons has been studied for the development of an on-line range monitoring apparatus. Specifically, within the PAPRICA (PAir PRoduction Imaging ChAmber) project [36], researchers have developed a novel 3D imaging technique, based on the Pair Production (PP) mechanism, occurring when prompt photons interact inside the detector itself. This photon detection technique is already

exploited in astrophysics telescopes [37]. The goal is to reconstruct the direction of origin both of the pair $e+-e-$ and of the photon which produced it, by measuring the 4-momentum of the two leptons. By analyzing the structure of PAPRICA in detail, three regions can be identified, as showed in Figure 2.2:

- Converter: it is the region in which an $e+-e-$ lepton pair is produced. It is made of a high Z material, and its thickness is such that it maximizes pair production, yet preventing the re-absorption of the produced leptons. The main problems are the high number of MCSs the pair undergoes in this region and the recoil of the nucleus involved in PP, which result in poor angular resolution $\Delta\theta$. Therefore, the reconstructed photon position is degraded ($\Delta\theta \sim 13°$), and the overall pair production efficiency results in the order of only 10%.

- Tracer: it is made of three pixelated layers of silicon, which reconstruct the traces of the pair.

- Calorimeter: in this region, the lepton pair stops and it is then absorbed. The measurement of the residual energy, using the calorimeter, makes it possible to solve the 4-momentum conservation equations and to reconstruct both the electron and positron trajectories, and that of the initial photon.

The aim of the MULTIPASS detector is to decrease uncertainties in the reconstruction of the original photon emission direction, reducing the error contribution due to MCSs. The detector will be made of layers of low Z scintillating fibers, improving angular resolution by a factor of ~ 2. In addition, the thin thickness of the fibers and the development of an ad hoc reconstruction algorithm will allow traces to be reconstructed with better accuracy. This, along with the detector's compactness and mobility, will ensure improved spatial accuracy for the entire tracking process.

2.1.3 The Detection of Neutrons: MONDO

As already mentioned in Section 2.1, the detection of neutron radiation represents a huge challenge in CPT, especially because of the presence of large intrinsic background and of low detection efficiency. Currently, only devices capable of measuring the total dose delivered by neutrons are available, but they do not provide detailed information about the neutrons themselves. In this matter, the greatest progress has

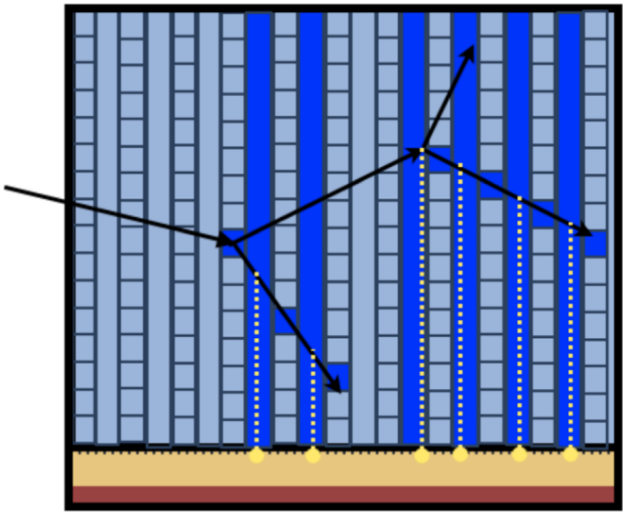

Figure 2.3: Schematic representation of the MONDO detector. Superimposed it is shown an event of double elastic scattering [38].

been made in the context of the MONDO (MOnitor for Neutron Dose in hadrOntherapy) [39] project. It aims to design a detector able to characterize the neutron flux, with the purpose of preventing tissue toxicity and the onset of secondary tumors. Furthermore, it would distinguish secondary neutrons leaving the patient's body from those resulting from the interaction of secondary particles with the surrounding environment. The structure of the detector is showed in Figure 2.3. It is made up of 800 layers, alternated along the x and y directions, of squared scintillating fibers with a side length of 250 µm, resulting in a total active volume of $16\times16\times20$ cm^3.

In order to trace the direction of origin and energy of the incident neutron, the idea is to exploit two successive scattering events, known as Double Elastic Scattering (DES), and to track recoil products, specifically high-energy protons, which can be easily detected with high spatial and energy resolution. The process is schematically showed in Figure 2.4. In an elastic scattering event, a neutron hits a proton, causing it to recoil. The neutron's momentum changes, and since 4-momentum is conserved, the proton is emitted with momentum which depends on the initial energy of the neutron, as shown in the following equations:

$$\mathbf{p}_n = \mathbf{p}_p \frac{1 + m_n/m_p}{2\cos\theta_p} \approx \frac{\mathbf{p}_p}{\cos\theta_p} \qquad \text{because } m_n \approx m_p \ , \tag{2.1}$$

and:

$$E_n = \frac{2E_p m_p}{\cos^2\theta\,(E_p + 2m_p + E_p/\cos^2\theta)} \approx \frac{E_p}{\cos^2\theta} \qquad \text{if } E_n << m_n\ , \tag{2.2}$$

where $(E_n,\ \mathbf{p}_n)$ is the initial neutron 4-momentum, $(E_p,\ \mathbf{p}_p)$ is the recoil proton 4-momentum, and θ_p is the angle identified by the direction of the two particles. A similar interaction occurs between the scattered neutron, of 4-momentum $(E'_n,\ \mathbf{p}_{n'})$ and a second recoiled proton, of 4-momentum $\left(E'_p,\ \mathbf{p}_{p'}\right)$, defining the angle $\theta_{p'}$. To reconstruct the track of the initial proton, first, $\mathbf{p}_p$ and $\mathbf{p}_{p'}$ must be determined through range measurements. Then, by evaluating the distance between the first and second interaction points, it is possible to retrieve the angle between the trajectory directions of the second neutron and the second recoil proton, $\theta_{p'}$. Using Equation 2.1, $\mathbf{p}_{n'}$ can be uniquely determined, just like $\mathbf{p}_n$, due to momentum conservation. Finally, θ_p can be calculated by applying Equation 2.1 once again.

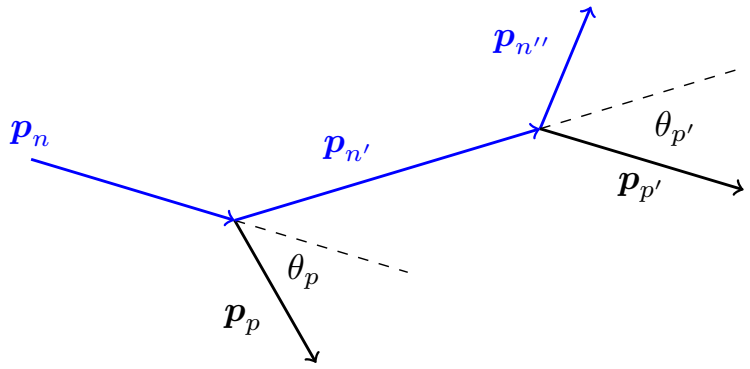

Figure 2.4: Schematic representation of a double elastic scattering event.

The MULTIPASS project proposes to employ the same technology developed for the MONDO detector in order to characterize in energy and emission angle neutrons produced by the primary beam in CPT. Thus, MULTIPASS will be able to detect simultaneously charged secondary fragments, prompt photons and neutrons, produced in the course of proton or ^{12}C treatments. The prototype will consist of layers of scintillating plastic fibers capable of capturing the light produced by the detected secondary products, and a dedicated read-out system will be able to provide inputs for the reconstruction algorithms.

2.2 The MULTIPASS Detector

2.2.1 The Structure of the Prototype

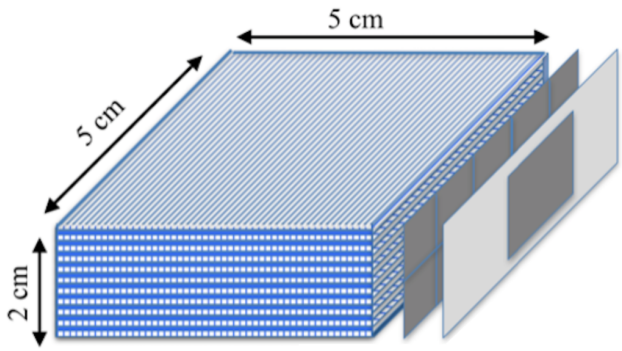

Figure 2.5: Sketch of the MULTIPASS detector.

As mentioned in the previous Section, the goal of the MULTIPASS project is to successfully overcome the limitations associated with the development of range monitoring techniques, encountered within the INSIDE, PAPRICA and MONDO projects. Structurally, the detector will be essentially similar to MONDO. It will consist of 40 planes of squared scintillating plastic fibers, 250 µm in side, made of EJ-200 (polyvinyltoluene), for a total volume of $5{\times}5{\times}2$ cm^3. Each plane contains two layers of fibers, with 200 fibers per plane, arranged in orthogonal planes along the x-y directions. Between the two layers of the plane, as well as at the entry and exit points of the detector, mylar spacers of 50 µm thickness will be positioned. 3D reconstruction will be later performed. Such a layout turns out to be functional both for an accurate study of the 3D reconstruction of prompt photon tracks, exploiting pair production, and for the tracking of protons coming from ion beam nuclear fragmentation or neutron DES. In particular, the thickness of the fibers is such that proton and $e+-e-$ tracks can be reconstructed with high spatial resolution and accuracy in energy measurement. The choice of plastic material is also significant. Indeed, being a highly hydrogenated substance, it maximizes the probability of interaction with a single proton in the case of elastic scattering, useful for neutron detection. At the same time, its low Z allows to reduce the $e+-e-$ MCS, allowing a better reconstruction of the trajectory of prompt photons, at the cost of reducing pair statistics due to the low PP cross section of $1 \div 10$ MeV prompt photons on

light material. The total active surface of the device will be small enough, of 5×5 cm^2, allowing it to be adapted to various treatment conditions and positioned close to the patient to increase the collectable statistics, thereby addressing gaps in detecting charged secondary fragments. Larger thickness (>> 2 cm) may be needed for prompt photons detection based on PP and for neutron tracking, reaching a total of 10×10×20 cm^3. An alternative approach could involve constructing a composite system consisting of multiple units, each similar to the one described in this Section. However, the prototype can be seen as a model of the final detector, varying its size once the associated electronics is properly developed.

2.2.2 The Read-out System

The use of fibers provides the compactness and technological features needed to track all processes of interest for MULTIPASS. However, it poses a huge challenge from the perspective of the read-out electronics. In fact, it must consist of a dedicated digital system with single-photon sensitivity (since the number of expected optical photons per MeV from a single fiber is of the order of 1 to 5 ph./MeV), in order to preserve the detector's granularity and increase the tolerated particle rate, thereby enhancing statistical acquisition. Being perfectly integrated to the sensor substrate, it will safeguard its compactness. The plan is to use a technology developed specifically for MONDO by Fondazione Bruno Kessler (FBK, Trento) and Centro Ricerche "Enrico Fermi" (CREF, Roma), the so-called SBAM (SPAD Based Acquisition for the MONDO experiment). It is based on the use of SPADs, semiconductor devices working through CMOS (Complementary Metal-Oxide-Semiconductor) technology. SPADs (Single Photon Avalanche Diodes) contain a high-doped p-n junction. When a photon impinges on the junction, it generates an electron-hole couple. These are directed by an intense electric field toward two electrodes. As they move, they ionize the matter they pass through, generating an avalanche reaction, which results in a detectable electrical signal, that can be acquired by the measurement system and stored in digital form. Acquisition ceases when the electric field is turned off.

Hitherto, electronics is being designed for the case of the MULTIPASS detector, as well as the trigger logic, the event selection and background rejection methods. Indeed, the SBAM technology perfectly adapts to all the requirements of the MULTIPASS project, thus representing a promising starting point.

Chapter 3

Monte Carlo Study of Secondary Particle Fluxes

As outlined in the previous chapter, the detector designed within the MULTIPASS project is quite complex. Its thickness is insufficient to observe with adequate statistical accuracy the DES events necessary for neutron detection. Moreover, while the reduced thickness and the low atomic number of the fiber material help minimize the MCS events experienced by the $e+ - e-$ lepton pair and the nuclear recoil, the total material budget would be too low to guarantee the detection of a significant number of pair production interactions due to the low PP cross section of photons in low Z material. Actually, the core of the project involves designing an innovative read-out electronics system, functioning of which can be tested on an actual detector model, albeit in a reduced size to keep production costs within reasonable limits. Once the electronics system is fully characterized, it will be adapted to a device of appropriate dimensions for actual therapeutic purposes.

The objective of this thesis work is to evaluate through Monte Carlo simulations, performed using the FLUKA code, the expected particle fluxes entering the detector during an hypothetical real treatment. Both protons and carbon ions have been simulated. The data obtained will be provided to the electronics team of the MULTIPASS project, to drive the design of the SPAD system, described in Section 2.2.2. In particular, this chapter presents the results of the performed simulations.

3.1 Details on the Simulations

3.1.1 The FLUKA Code

Monte Carlo simulations were conducted using the FLUKA[1] (FLUktuierende KAskade) code [40] [41]. This very versatile code, developed by INFN (Istituto Nazionale di Fisica Nucleare) and CERN (Conseil Européen pour la Recherche Nucléaire), consists of approximately 500,000 lines of FORTRAN code. It can simulate up to 60 different types of particles in a very wide energy range, up to 20 TeV, and their interaction with matter. For this reason, it is utilized in various fields, ranging from medical physics to astrophysics. FLUKA is able to follow the processes each simulated particle goes through, recording the type, instant and position of the interaction, and to establish the kinematic parameters of the outgoing particles. In addition, it also makes it possible to simulate the environment where phenomena occur, modeling the experimental geometries and assigning the appropriate constituent materials to every region. For this purpose, the software exploits an optimized Combinatorial Geometry (CG). FLUKA also offers the option of including or not the tracking of particular processes in the course of the simulation, possibly setting threshold energies. Another software, called Flair (FLUKA Advanced Interface) [42], serves as graphical interface of FLUKA, enabling the user to view and edit the inputs of the various simulations.

3.1.2 The Simulation Process

The simulation process can be viewed as a step-by-step procedure. First, it deals with the preparation of the geometry of the problem, contained in a text file where the user defines in space the various physical regions, depending on the experimental conditions. FLUKA CG is based on two main units: bodies and regions. Bodies define convex solid volumes spatially delimited by planar or quadratic surfaces. Once the space has been properly subdivided, regions can be defined, which result by applying logical operations, such as union, subtraction, and intersection, to bodies. This way, it is possible to construct, for example, the target, the detector and any other region of the setup. Regions need not be simply connected, or, otherwise said,

[1] FLUKA Home Page: `http://www.fluka.org/fluka.php`

they may be made of different parts, but should be uniform in their composition. Since FLUKA is not able to track particles beyond the outermost border, the experimental setup must be surrounded by an ideal absorber material, named blackhole, which absorbs every escaping particle. Moreover, inside the boundary determined by the blackhole, every point must belong to one single region.

Then, the actual simulation input file is created. It is a text file containing all the details of the processes to be computed, specified by FLUKA's option lines, known as cards. Cards all have the same structure, characterized by seven fields, which the author of the file fills in as needed, with default options. For instance, cards can define the energy and the origin point of the impinging particle beam, the materials assigned to the various regions, the phenomena to be taken into account during the simulation, along with possible threshold values, and particularity related to the information acquisition of the simulated processes. As FLUKA interfaces are fixed and the number of data to be handled, once the simulation runs, is extremely large, in order to appropriately follow the processes particles go through on their way inside the target and record only the information of interest in a personalized way, an ad hoc set of codes was developed, the so named routines, brute output of which is a truly massive data file. The output file of the simulation is organized in three main sections: the first, dedicated to describe the physical and kinematic information of every produced particle; the second, which collects everything linked to particle crossings between different regions; the third, which quantifies the energy releases in the different active parts of the detector.

Then, the direct output of the FLUKA simulation is reprocessed by a dedicated C++ code, which produces a ROOT file. This file records basic information about the produced particle flux, as defined in the routines, in suitable histograms. ROOT[2] is a software written in FORTRAN developed by CERN which is able to follow the complex processes the simulated particles go through and easily record the large amount of data associated.

The final step consists of data analysis, leading to the creation of the final ROOT file, using a C++ code. Starting from the previous ROOT file, it reorganizes the data to address the particular problem being studied. In this way, it is possible to trace, for example, the energy distribution of a single particle type or studying only

[2]ROOT Home Page: `https://root.cern/`

the crossing between two specific regions.

In this thesis work, the simulation process has been addressed in all its aspects.

3.2 Study with a PMMA Target

In the first part of the work, the geometry employed was very simple. The objective of this preliminary study was not only to compute the production statistics per single pencil beam, but also to analyze how particle fluxes at the entrance of the detector varied as a function of the angular positioning of MULTIPASS.

Simulations were performed using a rectangular PMMA (polymethylmethacrylate) target. PMMA, chemical formula of which is $(C_5O_2H_8)_n$, is a transparent and durable plastic polymer, which is radiologically equivalent to human tissue. Therefore, it is widely used to simulate the interaction processes with biological matter. The target has dimensions of $5\times5\times20$ cm^3 and is centered with respect to the FLUKA origin along the x and y directions. Along the z-axis, it is appropriately shifted so that the FLUKA origin coincides with the position of the Bragg peak of the simulated beam. The positioning of the target is shown in Figure 3.1.

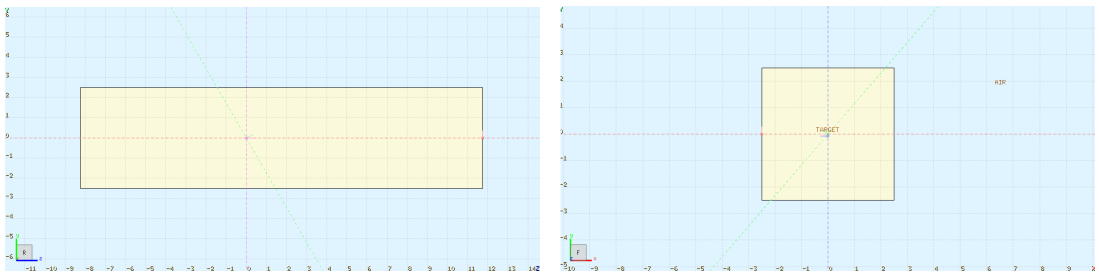

Figure 3.1: Left: Flair y-z view of the PMMA target. Right: Flair x-y view of the PMMA target.

To design the detector geometry, the FLUKA LATTICE option was used, which allows for the construction of modular structures repeated in space, as shown in Figure 3.2. In this case, the module consists of a plane including two layers of fibers, aligned along the x and y directions respectively and separated by a layer of mylar. It is defined in a distinct region, called PARKfib, and described in full detail in terms of bodies and regions. The region actually occupied by the detector is defined using a series of 40 LATTICE cells, which will contain the replications of the basic unit. To establish the relationship between the main module and the lattice,

a sequence of transformations, specifically rotations and translations, is defined. These transformations ensure that each point of the unit is correctly mapped to a corresponding point within the detector's region. Besides the convenience from a programming standpoint, this technique offers another significant advantage. The interaction process inside a specific detector plane is always simulated within the basic unit contained in PARKfib. This approach allows the LATTICE cells to be treated as distinct entities, maintaining the detector's physical accuracy, while benefiting from the computational efficiency of defining only the fundamental unit and its replication rules. Finally, to improve the accuracy of the scenario, the FLUKA region where the experimental setup was developed was designated as air, which then surrounds the target and the detector.

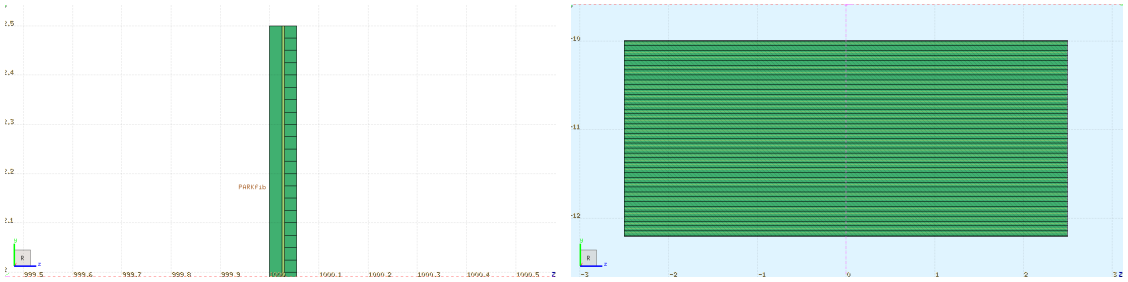

Figure 3.2: Left: Constituent module of the detector, within PARKfib, taken from Flair. Each plane consists of two layers of fibers and an intermediate thick of mylar. Right: Flair representation of the detector, obtained from the juxtaposition of different modules.

Simulations were conducted using a primary beam of $5 \cdot 10^7$ carbon ions, mono-energetic, with an energy of 220 MeV/u , and the Bragg peak in PMMA occurring at a depth of 8.25 cm. This depth corresponds to the forward displacement of the target along the z-axis relative to the origin of the FLUKA coordinate system. In order to preserve the constructed geometry, the energy of the protons was selected to ensure that the position of the Bragg peak remained unchanged. Using the NIST (National Institute of Standards and Technology) XCOM database, which provides the range of protons at various energies within different materials, the corresponding energy was determined to be 112.3 MeV. In this case as well, the beam used was mono-energetic, for a total of $5 \cdot 10^7$ particles. It is worth noting that the energies chosen for both carbon ions and protons are reasonable, as they fall perfectly within the range used for therapeutic purposes. In both cases, the primary beam (pencil

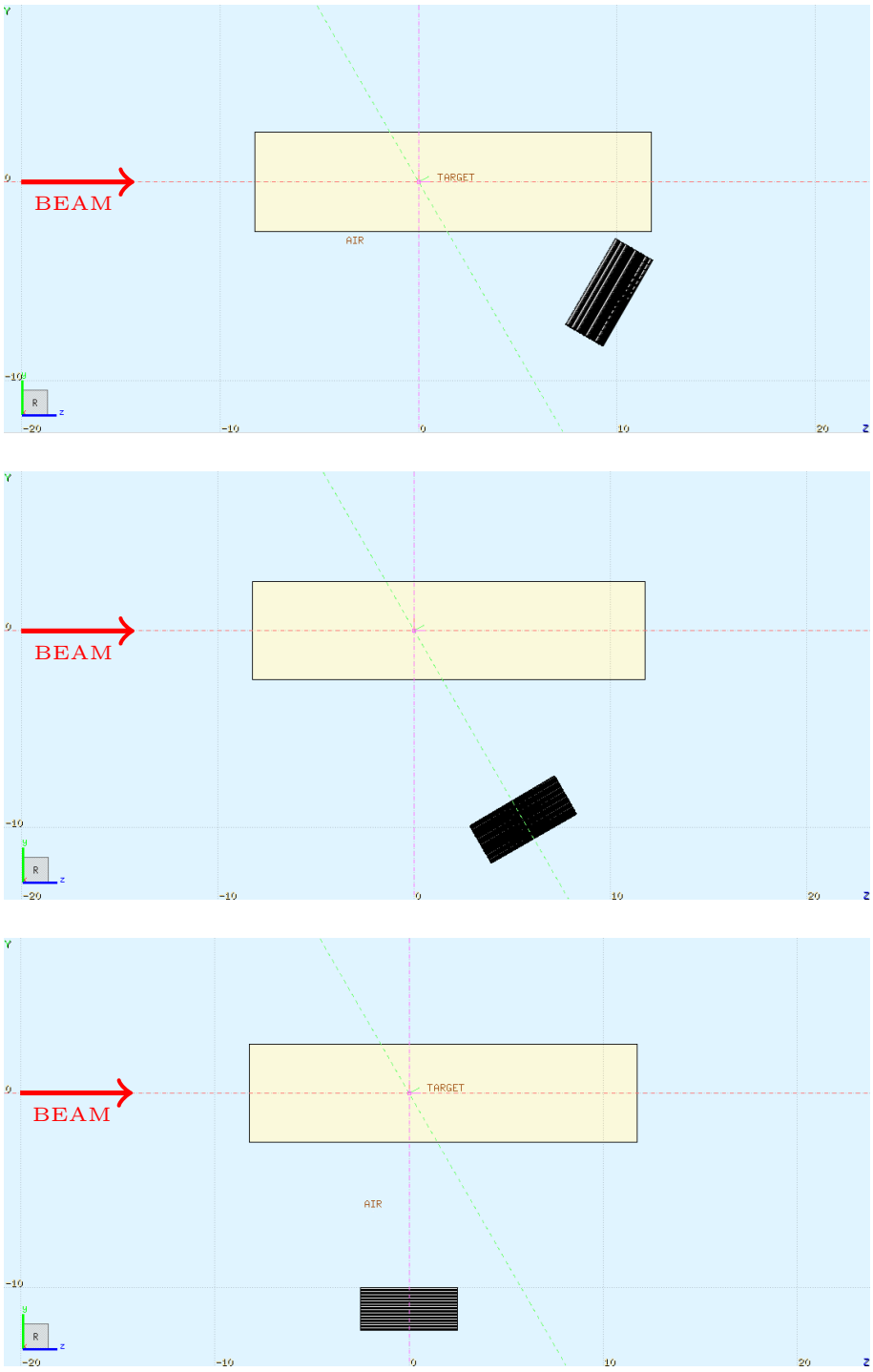

Figure 3.3: Flair representation (y-z plane) of the positioning of MULTIPASS, shown in black, rotated by 30°, 60°, and 90° with respect to the z-axis. The PMMA target is shown in yellow. The pencil beam (red arrow) is coming from z = -20 cm, having a z-positive direction.

beam) was delivered at the center of the target lateral face, the one positioned along the x-y plane, from -20 cm along the z-axis with respect to the FLUKA center. In these initial simulations, no triggers were applied, allowing all simulated events to be saved in the FLUKA output. This approach was intentionally chosen to maintain the broadest scenario possible, being interested in the most general information from the simulation.

The detector's angular position was adjusted to assess the expected fluxes of incoming particles at different angles. Both for simulations with protons and carbon ions, configurations at rotation angles around the x-axis of 30°, 60°, and 90° with respect to the z-axis (refer to Figure 3.3) were analyzed, obtaining histograms for the three particle types of interest: protons, neutrons and photons. The kinetic energy and the polar angle (identified with respect to the direction of the primary beam) distribution of the particles produced at different simulation levels have been studied:

- At the particle generation, within the PMMA target;
- At the target-air crossing, to study the particles exiting the target;
- At the air-detector crossing, to study the particles entering MULTIPASS.

The distance between the detector and the target center, specifically from the FLUKA origin, was set to 10 cm. Thus, the solid angle covered by the detector was of 0.02 sr.

Particles' kinetic energy was calculated using the relativistic kinetic energy formula (expressed in natural units):

$$E_{k_i} = \sqrt{p_{x_i}^2 + p_{y_i}^2 + p_{z_i}^2 + m_i^2} - m_i \ , \tag{3.1}$$

where E_{k_i}, p_{x_i}, p_{y_i}, p_{z_i} and m_i are the kinetic energy, the momentum components and the mass of the i-th particle. The kinetic information of the particles is saved in the customized FLUKA output (see Section 3.1.2). With regard to the definition of the values of polar angle, once the direction identified by the momentum of the i-th particle is determined as a ROOT TVector3, the corresponding polar angle can be extracted using the .Theta() method from the TVector3 class in ROOT [3].

[3]See `https://root.cern.ch/doc/master/classTVector3.html` for details.

For the purposes of this study, data related to the particle fluxes per primary particle Φ_{gen} at generation within the PMMA target, $\Phi_{PMMA-air}$ at the PMMA-air crossing, and $\Phi_{air-det}$ at the air-detector crossing were extracted, specifically the ratios:

$$\Phi_{gen} = \frac{n^i_{gen}}{n_{prim}} \qquad \Phi_{PMMA-air} = \frac{n^i_{PMMA-air}}{n_{prim}} \qquad \Phi_{air-det} = \frac{n^i_{air-det}}{n_{prim}} \ , \tag{3.2}$$

where n_{prim} is the number of simulated primaries, n^i_{gen}, $n^i_{PMMA-air}$ and $n^i_{air-det}$ are the number of particles of the i-type (protons p, neutrons n or photons γ), at generation, at the PMMA-air crossing and at the air-detector crossing, respectively.

3.2.1 Simulations with Protons

In this Section, the results obtained from proton simulations are presented. For the purposes of this work, which focuses on the analysis of secondaries for range monitoring, only direct daughter particles of the simulated primaries have been considered. To extract the number of particles to be considered in each of the three simulations presented in Section 3.2, it is necessary to compute the integral of the kinetic energy distribution. The corresponding values are displayed in the box adjacent to each histogram, labeled as *Integral*. Since particles with energies that are too low would not be detected, energy thresholds have been applied: 5 MeV for protons and 10 MeV for neutrons. Instead, at this stage of the study, it was not necessary to apply any energy threshold cut for photons. This procedure can be applied to study the generation process, the PMMA-air crossing and the air-MULTIPASS crossing.

	Production $[\#i/n_{prim}]$	PMMA-air crossing $[\#i/n_{prim}]$
p ($E_k^{\mathrm{gen}_p} > 5$MeV)	$1.166 \cdot 10^{-1}$	$1.798 \cdot 10^{-3}$
n ($E_k^{\mathrm{gen}_n} > 10$MeV)	$2.724 \cdot 10^{-2}$	$2.246 \cdot 10^{-2}$
γ	$2.204 \cdot 10^{-3}$	$1.942 \cdot 10^{-3}$

Table 3.1: Flux of protons, neutrons, and photons at production within the PMMA target and at the crossing PMMA-air in proton simulations. The number of simulated primaries is $5 \cdot 10^7$.

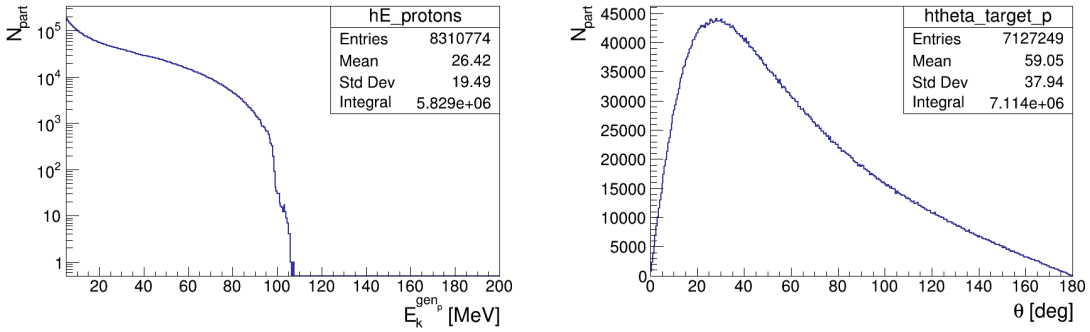

Figure 3.4: Kinetic energy (left) and polar angle (right) distributions of protons at production within the PMMA target in proton simulations. Observe the shape of the energy distribution and the peak at lower angles. Logarithmic scale was used on the y-axis for the energy histogram.

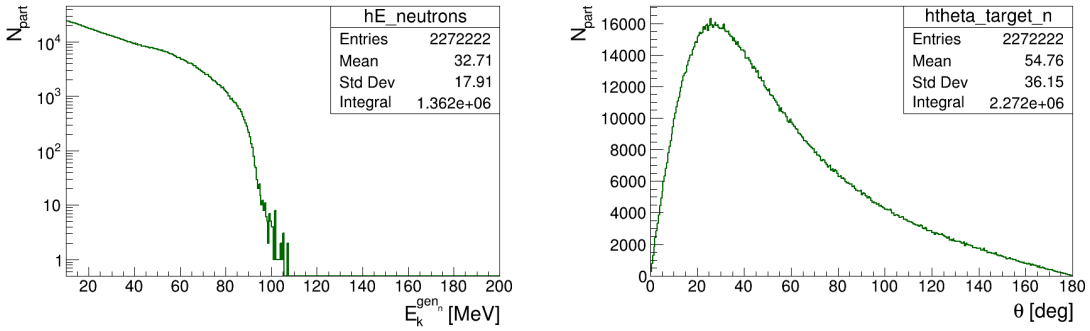

Figure 3.5: Kinetic energy (left) and polar angle (right) distributions of neutrons at production within the PMMA target in proton simulations. Observe the shape of the energy distribution and the peak at lower angles. Logarithmic scale was used on the y-axis for the energy histogram.

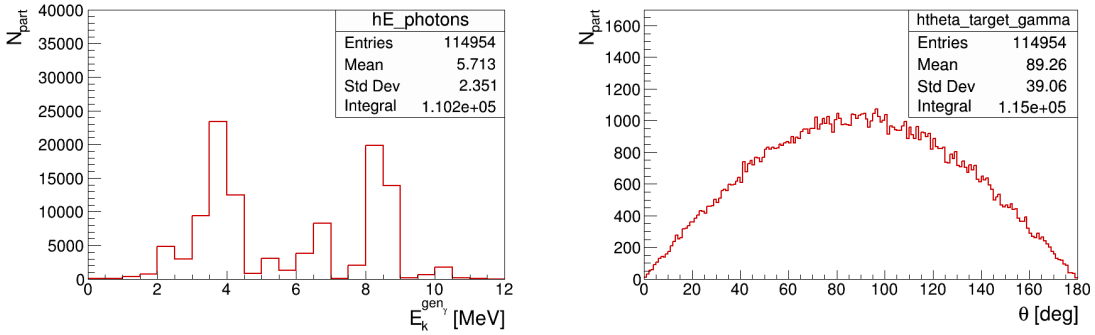

Figure 3.6: Kinetic energy (left) and polar angle (right) distributions of photons at production within the PMMA target in proton simulations. Note the peaks in the energy spectrum (especially, the 4.44 MeV one) and the symmetry of the angular distribution.

To ensure better readability, all energy distributions presented for protons and neutrons are shown with a logarithmic scale on the y-axis.

Figures 3.4, 3.5 and 3.6 show, on the left, the kinetic energy distributions related to protons, neutrons and photons, respectively, at production within the PMMA target. Table 3.1 reports the flux of secondaries at generation within the PMMA.

The kinetic energy distribution for protons and neutrons show a decreasing trend in the initial region, followed by a rapid drop. Specifically, the curve slopes down at around 110 MeV, which is close to the energy of the simulated primary particles. This trend is reasonable, since, in the course of a protontherapy treatment, secondary protons and neutrons arise from elastic scattering interactions. Thus, the maximum energy that the produced particles can have will be at most equal to that of the primary proton beam. Instead, the photon spectrum shows characteristic peaks corresponding to the de-excitation energies of the excited target nuclei, among which the one at ~ 4.44 MeV corresponds to the de-excitation peak of ^{12}C.

The production statistics is robust. The number of particles of each species generated within the PMMA is in the order of $10^5 - 10^6$. However, by applying the low-energy cut-off, significant differences emerge between the actual number of generated protons and neutrons and the number of secondaries above the threshold energy, especially for neutrons. In fact, in this case, the total number above threshold results almost halved. This occurrence underscores that a considerable fraction of the secondary particles produced are at low-energy.

Figures 3.4, 3.5 and 3.6 show, on the right, the polar angle distributions of protons, neutrons and photons, respectively, at generation within the PMMA target.

In the case of protons and neutrons, an emission peak is observed at small angles, at $\sim 30°$. This phenomenon reflects the characteristics of high-energy scattering. In particular, the interaction processes that protons and neutrons undergo depend on the size of the impact parameter. When the parameter is small, after an elastic interaction, the projectile continues its forward path through the target. In fact, in the case of elastic scattering, since the projectile is a high-energy particle and travels much faster than the target it interacts with, the interaction time between the two is very short. As a result, only a very small fraction of the incident particle's momentum is transferred to the target, and the particle continues its motion in the direction of incidence with nearly the same initial velocity. In contrast, if the impact

parameter is larger, the trajectory is deflected and the scattered particle is emitted at wider angles. In general, as consequence of momentum conservation, the more energetic particles are emitted at small angles, while the less energetic ones are emitted at larger angles. The emission pattern suggests that a significant portion of the generated particles is emitted forward, though the broadness of the distribution indicates that also a considerable fraction is produced at larger angles.

On the other hand, as expected, the photon emission spectrum is symmetric, indicating that their emission is isotropic. Photons are mainly emitted from nuclear de-excitation. The direction of photon emission depends on the orientation of the nuclear spin, which, in the absence of perturbations, will be randomly oriented. Therefore, the photon will not be emitted in any preferential direction.

Figures 3.7, 3.8 and 3.9 exhibit the distributions of kinetic energy and polar angle for protons, neutrons, and photons, respectively, at the PMMA-air crossing, while Table 3.1 contains the flux of secondaries at the PMMA-air crossing.

When examining the number of particles at the target-air crossing, a significant reduction in the number of protons exiting the target can be observed, approximately by two orders of magnitude. In fact, protons are electrically charged, unlike neutrons and photons, and they transfer energy to the medium according to the Bethe-Bloch formula. For this reason, a significant fraction of them, especially among the low-energy ones, is absorbed by the medium, although the thickness they have to traverse is quite small. In contrast, the number of neutrons and photons that successfully exit the PMMA remains high, in the order of about $10^5 - 10^6$, as the number of protons and neutrons produced.

Figures 3.10 and 3.11 show the 2D histograms, with the polar angle values on the x-axis and the kinetic energy values on the y-axis, related to the proton and neutron crossing at the PMMA-air interface, respectively. It can be observed that most protons are emitted at angles between 20° and 80°. No protons are observed exiting the PMMA below 20°, as, due to the considerable length of the target, most of them are absorbed before exiting the material. In contrast, neutrons are emitted at any angle, but mainly between 40° and 60°.

The most interesting aspect is related to the data concerning the air-MULTIPASS crossing. Figures 3.12, 3.13 and 3.14 depict the overlap of the plots of kinetic energy and polar angle for protons, neutrons, and photons, respectively, in the three

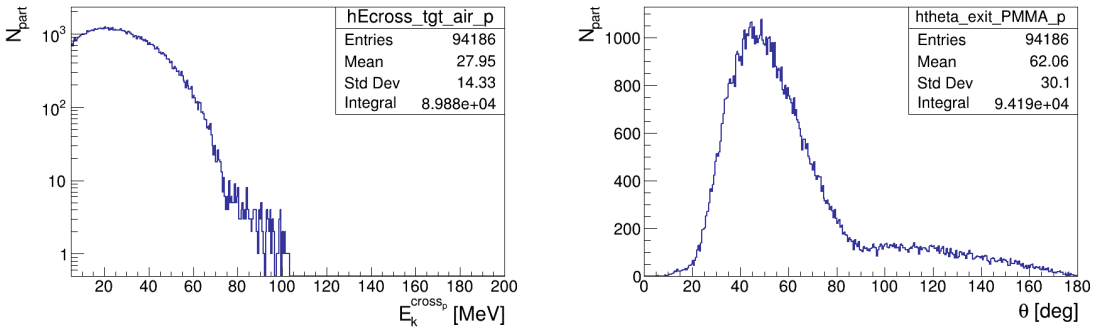

Figure 3.7: Kinetic energy (left) and polar angle (right) distributions of protons at the PMMA-air crossing in proton simulations. Logarithmic scale was used on the y-axis for the energy histogram.

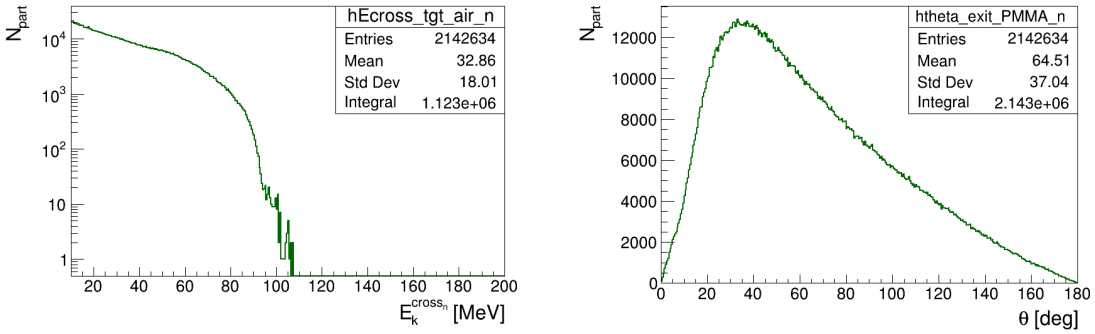

Figure 3.8: Kinetic energy (left) and polar angle (right) distributions of neutrons at the PMMA-air crossing in proton simulations. Logarithmic scale was used on the y-axis for the energy histogram.

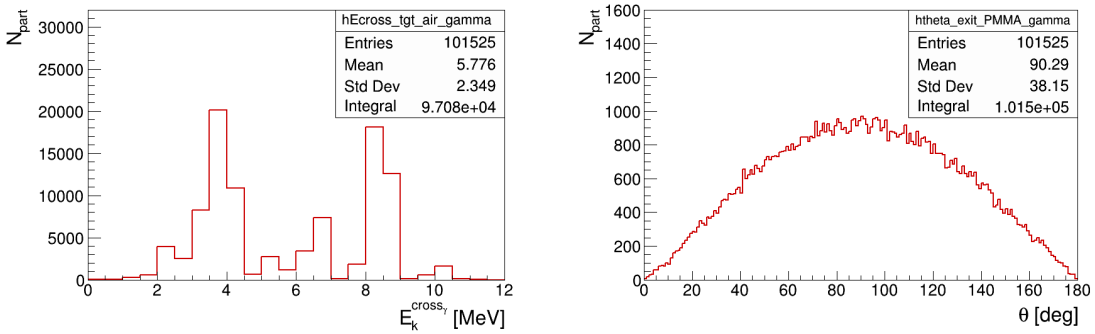

Figure 3.9: Kinetic energy (left) and polar angle (right) distributions of photons at the PMMA-air crossing in proton simulations.

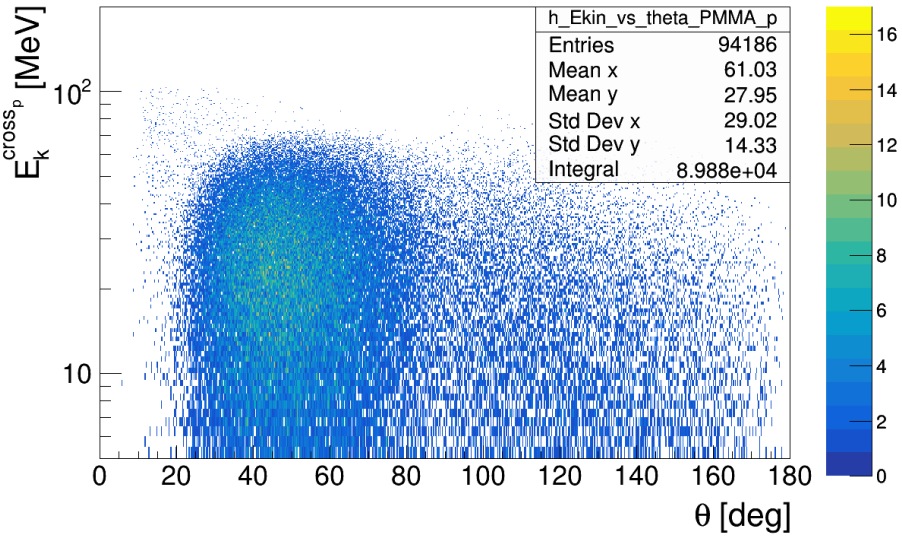

Figure 3.10: 2D histogram displaying the polar exit angle values on the x-axis and the corresponding kinetic energy at the PMMA-air crossing on the y-axis for protons in proton simulations. Most protons exit the target between 20° and 80°. Logarithmic scale was used on the y-axis.

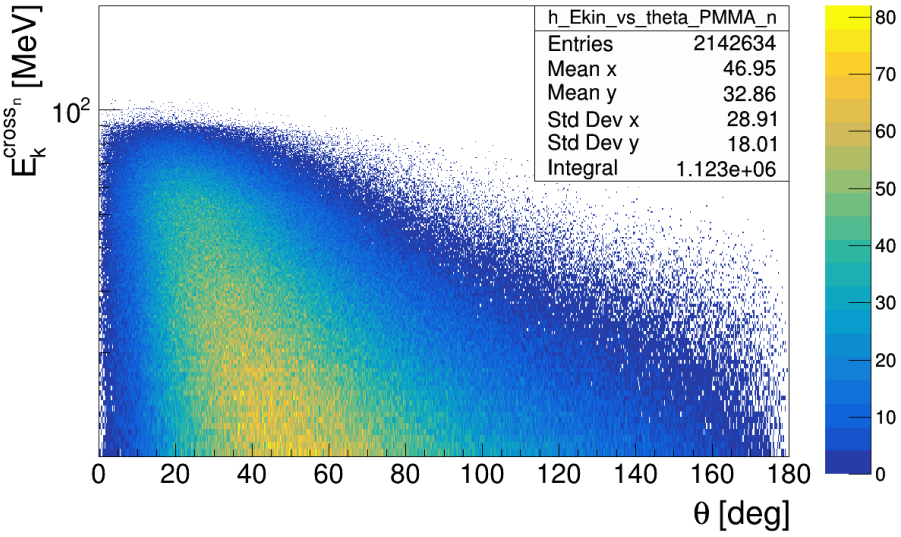

Figure 3.11: 2D histogram displaying the polar exit angle values on the x-axis and the corresponding kinetic energy at the PMMA-air crossing on the y-axis for neutrons in proton simulations. Most neutrons exit the target between 40° and 60°. Logarithmic scale was used on the y-axis.

angular configurations at the air-detector crossing, while Table 3.2 presents the flux of secondary particles at the air-detector crossing.

	30° $[\#i/n_{prim}]$	60° $[\#i/n_{prim}]$	90° $[\#i/n_{prim}]$
p ($E_k^{\text{cross}_p} > 5\text{MeV}$)	$5.640 \cdot 10^{-6}$	$7.368 \cdot 10^{-5}$	$6.562 \cdot 10^{-5}$
n ($E_k^{\text{cross}_n} > 10\text{MeV}$)	$1.051 \cdot 10^{-3}$	$6.396 \cdot 10^{-4}$	$3.004 \cdot 10^{-4}$
γ	$1.818 \cdot 10^{-5}$	$2.176 \cdot 10^{-5}$	$2.910 \cdot 10^{-5}$

Table 3.2: Flux of protons, neutrons, and photons at the air-MULTIPASS crossing in proton simulations. The number of simulated primaries is $5 \cdot 10^7$.

A relevant fraction of neutrons reaches the detector, and this number increases when moving from the 90° configuration to the 30° one. However, this behavior is not observed for protons, as at 30° the number of entering particles is significantly lower compared to the other two configurations. This is due to a re-absorption effect. By decreasing the angle at which the detector is positioned, protons must travel a greater distance to exit the PMMA. While this effect is not noticeable at 60°, at 30° it causes significant absorption of protons within the target, resulting in a reduction of the number of protons that actually reach the detector. This result highlights how, in the case of proton treatments, positioning the detector at small angles is ineffective. This finding aligns well with real therapeutic situations, where the placement of range monitoring detectors cannot be done at small angles due to the presence of the patient's body in the vast majority of the cases. In general, range monitoring during proton treatments is quite complex, as positioning at large angles involves detecting protons emitted at wider angles due to elastic scattering. These protons are low-energy, and, since a significant portion is absorbed before exiting the target, the statistics entering the detector is always low. The situation, however, improves in the case of treatments using carbon ions, as will be discussed in Section 3.2.2.

Regarding photons, those with energy below 2 MeV are absorbed, as observed by comparing Figures 3.6 and 3.14; however MULTIPASS is not concerned with the detection of photons in that energy range. Note that the incoming fluxes remain nearly identical across the three angular configurations.

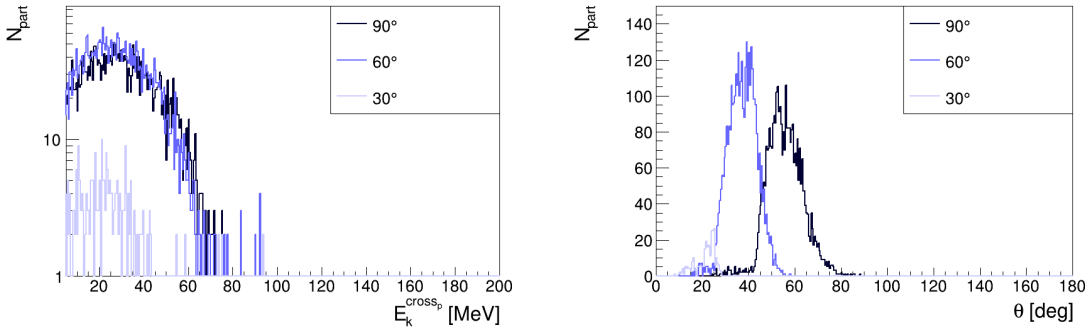

Figure 3.12: Kinetic energy (left) and polar angle (right) distributions of protons at the air-MULTIPASS crossing in the three angular configurations in proton simulations. As can be seen from the histograms corresponding to the 30° configuration, the absorption effect causes the suppression of the number of particles entering the detector. Logarithmic scale was used on the y-axis for the energy histogram.

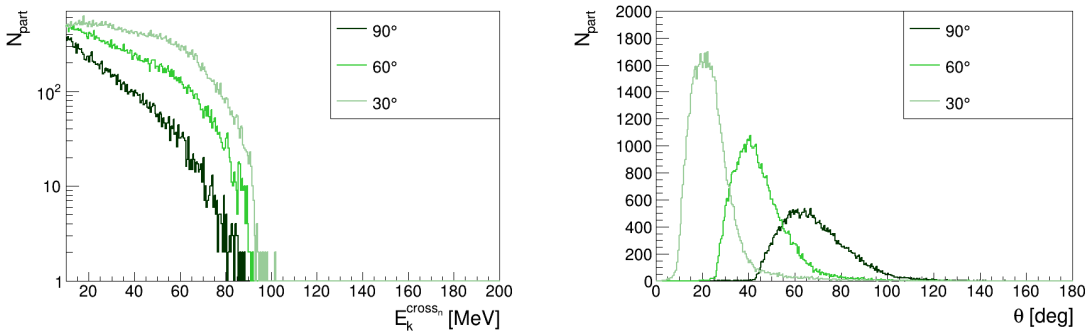

Figure 3.13: Kinetic energy (left) and polar angle (right) distributions of neutrons at the air-MULTIPASS crossing in the three angular configurations in proton simulations. Logarithmic scale was used on the y-axis for the energy histogram.

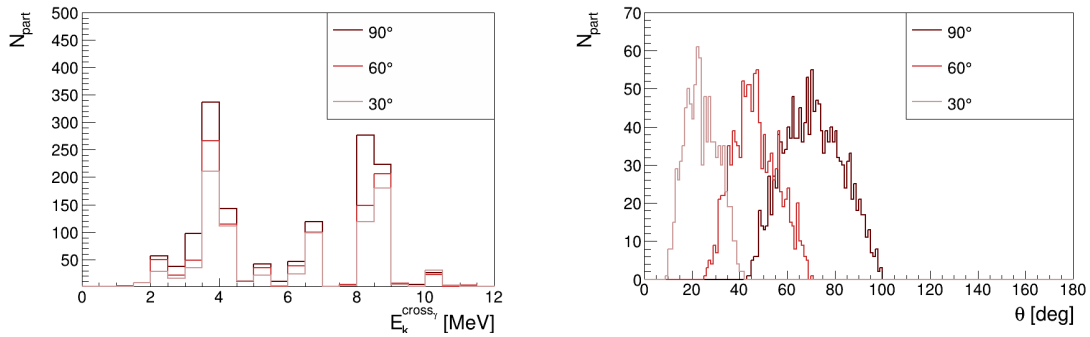

Figure 3.14: Kinetic energy (left) and polar angle (right) distributions of photons at the air-MULTIPASS crossing in the three angular configurations in proton simulations.

3.2.2 Simulations with Carbon Ions

As in the case of protons, this Section presents the results of the simulations with carbon ions related to the distributions of kinetic energy and polar angle of secondary particles, directly produced by the primary beam. The geometry used is the same as in the previous case, described in Section 3.2, as is the number of primary particles simulated, specifically $5 \cdot 10^7$ carbon ions at an energy of 220 MeV/u.

	Production $[\#i/n_{prim}]$	PMMA-air crossing $[\#i/n_{prim}]$
p ($E_k^{\text{gen}_p} > 5\text{MeV}$)	$8.476 \cdot 10^{-1}$	$2.374 \cdot 10^{-1}$
n ($E_k^{\text{gen}_n} > 10\text{MeV}$)	$6.848 \cdot 10^{-1}$	$5.912 \cdot 10^{-1}$
γ	$1.009 \cdot 10^{-2}$	$8.658 \cdot 10^{-3}$

Table 3.3: Flux of protons, neutrons, and photons at production within the PMMA target and at the crossing PMMA-air in carbon simulations. The number of simulated primaries is $5 \cdot 10^7$.

Again, to ensure an appropriate reading of the reported graphs, the logarithmic scale was used on the y-axis for all energy plots related to protons and neutrons.

Starting from the production histograms, Figures 3.15, 3.16 and 3.17 show the kinetic energy and polar angle distributions related to protons, neutrons and photons, respectively, at generation within the PMMA target, while Table 3.3 reports the fluxes of protons, neutrons and photons at production.

The trends closely align with those obtained in proton simulations. However, meaningful differences can be highlighted. It is clear that the energy at which particles are produced within the PMMA is significantly greater than in the case of simulations with protons, reaching values of up to 1000 MeV, since a carbon ion at 220 MeV/u corresponds to a total energy per ion of 2640 MeV. Moreover, the effects of the interaction with the target will be more severe and pronounced, leading to the generation of a larger number of secondary particles. Indeed, in this scenario, protons and neutrons are produced not only through elastic scattering, but also via projectile fragmentation, and tend to retain the velocity and trajectory of the original particle, as discussed in Section 1.3.1. This phenomenon ensures that the number of protons and neutrons generated increases by a factor of approximately 10 with respect to the case of 112.3 MeV proton beam, and that their energy and velocity remain comparable to those of the primary particle.

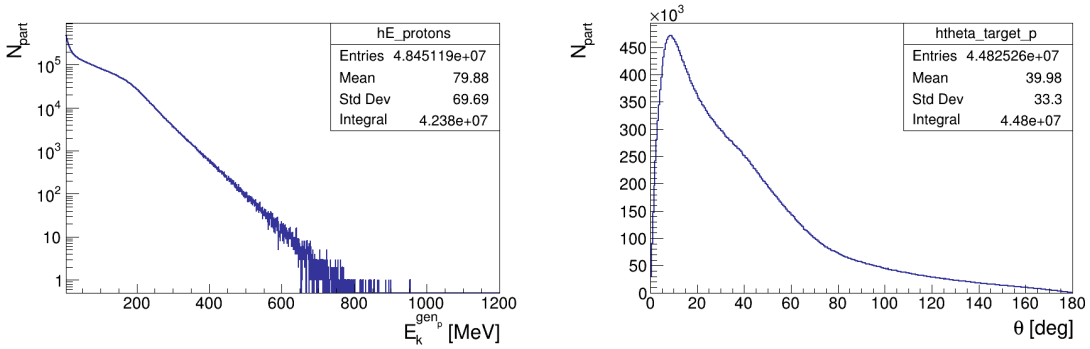

Figure 3.15: Kinetic energy (left) and polar angle (right) distributions of protons at production within the PMMA target in carbon simulations. Note the higher proton energy and the narrower θ distribution peak at smaller angles compared to proton simulations. Logarithmic scale was used on the y-axis for the energy histogram.

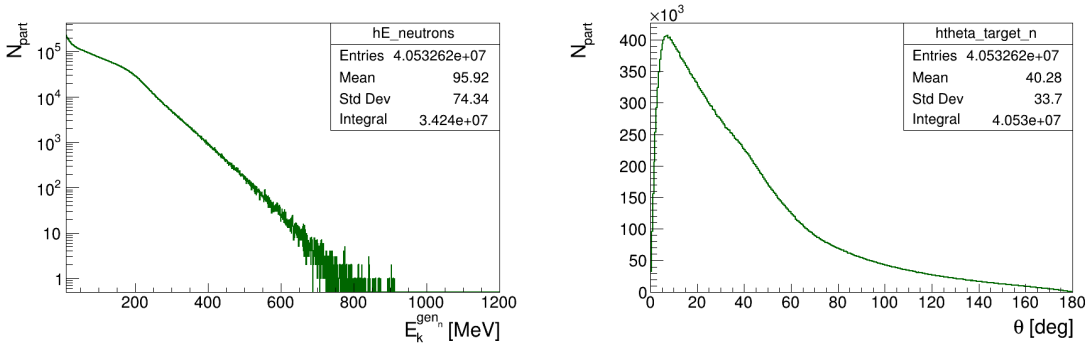

Figure 3.16: Kinetic energy (left) and polar angle (right) distributions of neutrons at production within the PMMA target in carbon simulations. Note the higher neutron energy and the narrower θ distribution peak at smaller angles compared to proton simulations. Logarithmic scale was used on the y-axis for the energy histogram.

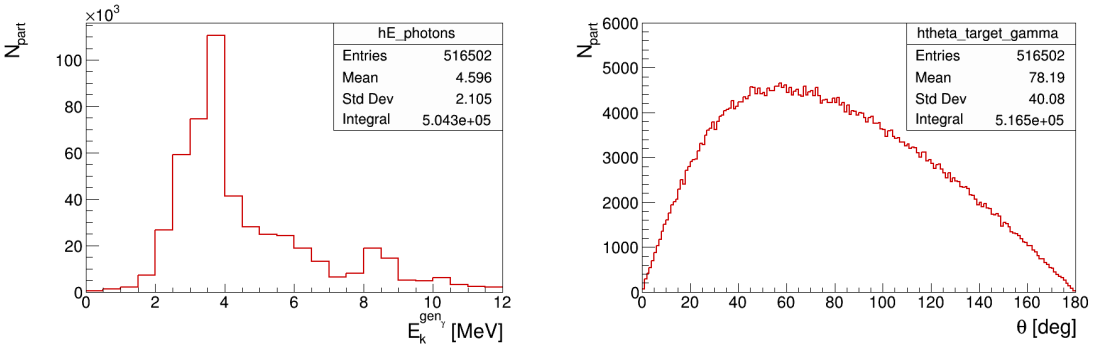

Figure 3.17: Kinetic energy (left) and polar angle (right) distributions of photons at production within the PMMA target in carbon simulations.

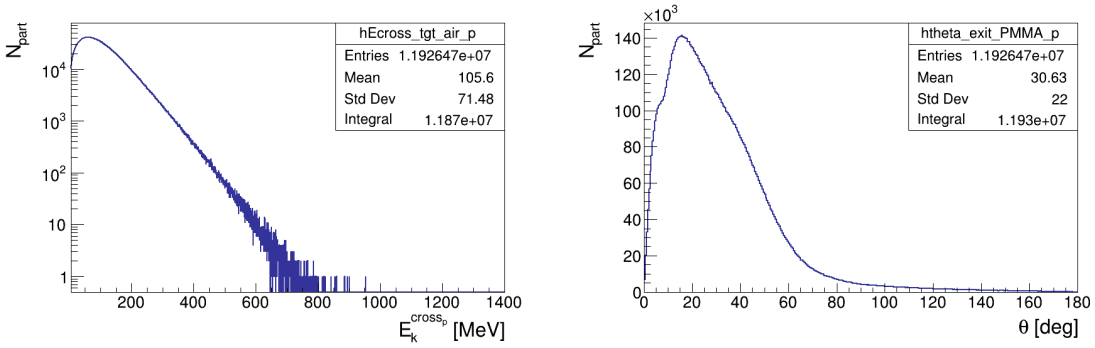

Figure 3.18: Kinetic energy (left) and polar angle (right) distributions of protons at the PMMA-air crossing in carbon simulations. Logarithmic scale was used on the y-axis for the energy histogram.

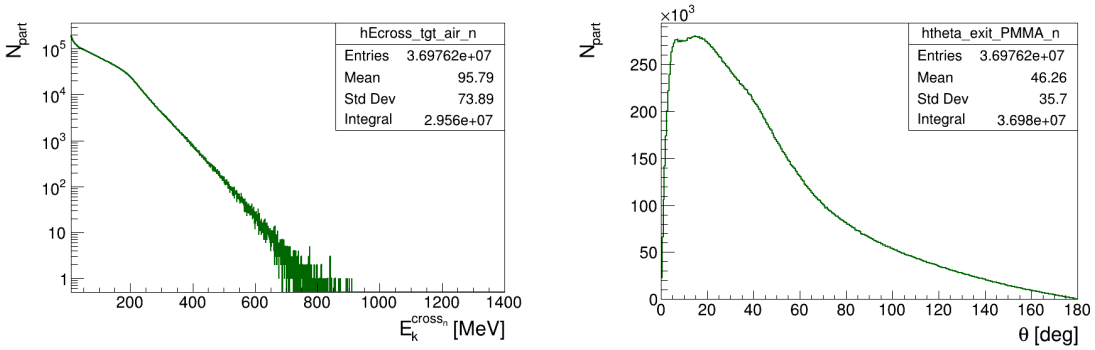

Figure 3.19: Kinetic energy (left) and polar angle (right) distributions of neutrons at the PMMA-air crossing in carbon simulations. Logarithmic scale was used on the y-axis for the energy histogram.

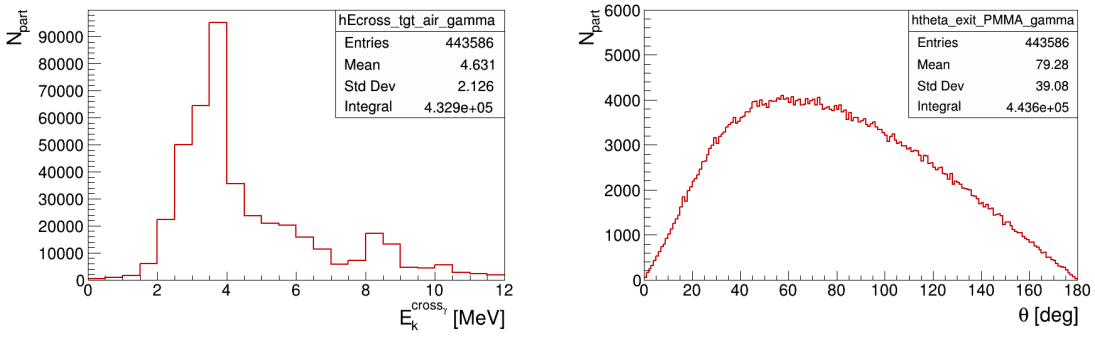

Figure 3.20: Kinetic energy (left) and polar angle (right) distributions of photons at the PMMA-air crossing in carbon simulations. Logarithmic scale was used on the y-axis for the energy histogram.

Another meaningful difference compared to the previous case lies in the narrower angular distribution of protons and neutrons generated in the PMMA target, which is also sharply peaked at smaller angles. Indeed, the fragments from the projectile, as mentioned below, tend to preserve the incidence direction of the primary beam. Therefore, a significant portion of protons and neutrons is emitted in the forward direction. The result is a peaked distribution at smaller angles relative to the proton case, as can be observed by comparing the corresponding average values reported in the statistics box.

Figures 3.18, 3.19 and 3.20 exhibit the kinetic energy and polar angle distributions related to protons, neutrons and photons, respectively, at the PMMA-air crossing, while Table 3.3 contains the particles' flux at the PMMA-air crossing.

It is evident that the fragmentation effect not only ensures that low-energy thresholds have minimal impact on production statistics, but also that the number of particles able to exit the target preserves almost the same order of magnitude as the particles produced. Figures 3.21 and 3.22 show the 2D histograms, with the polar angle values on the x-axis and the kinetic energy values on the y-axis, related to the proton and neutron crossing at the PMMA-air interface, respectively. In the case of protons, the yellow region highlights how a significant component of high-energy particles is emitted at small angles. These derive from the fragmentation of the projectile and, as explained earlier, are predominantly emitted forward. In contrast, for neutrons, there is only a small peak of high-energy neutrons resulting from projectile fragmentation, while a considerable lower-energy fraction is emitted at larger angles, between 40° and 60°. This profile, which is consistent with that of neutrons at the PMMA-air crossing observed in simulations with protons (see Figure 3.8), emphasizes that they are emitted following elastic scattering interactions.

It is interesting to observe the plots related to secondary particles at the air-detector crossing, depicted in Figure 3.23, 3.24 and 3.25. Table 3.4 presents the flux of protons, neutrons and photons at the air-detector crossing.

The flux of incoming particles is significantly higher with respect to the case of proton simulations, due to the greater energy and the larger number of secondary particles produced. Unlike the simulations with protons, this phenomenon is valu-

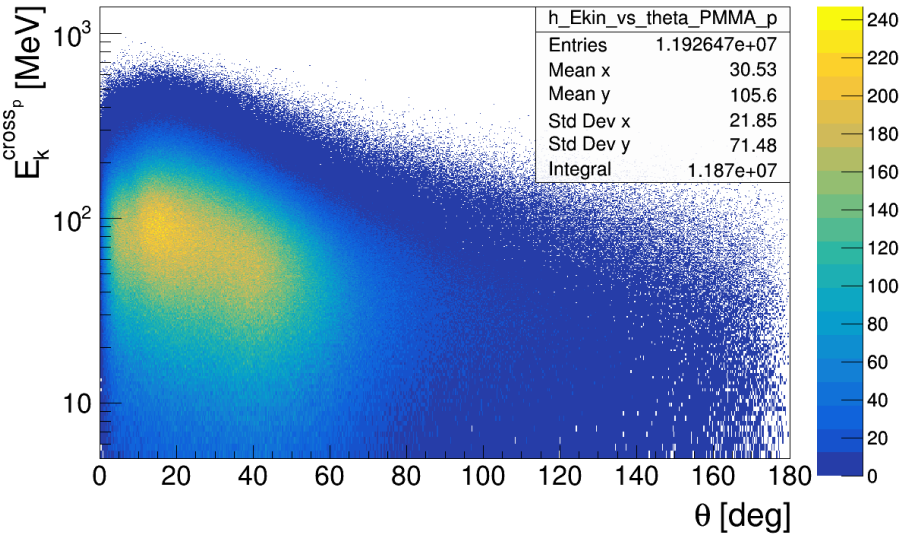

Figure 3.21: 2D histogram displaying the polar exit angle values on the x-axis and the corresponding kinetic energy at the PMMA-air crossing on the y-axis for protons in carbon simulations. In yellow, the high-energy proton component emitted forward due to projectile fragmentation. Logarithmic scale was used on the y-axis.

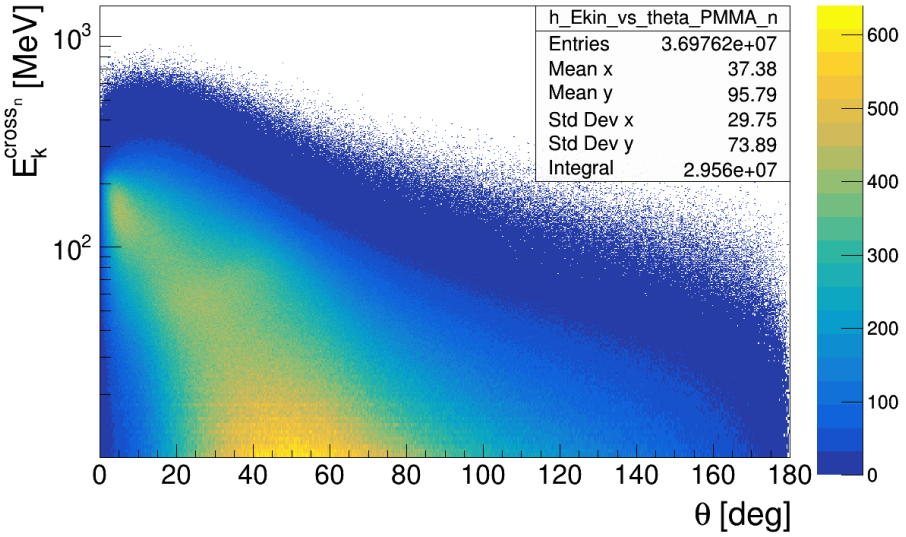

Figure 3.22: 2D histogram displaying the polar exit angle values on the x-axis and the corresponding kinetic energy at the PMMA-air crossing on the y-axis for neutrons in carbon simulations. Observe the significant emission of neutrons between 40° and 60°, resulting from elastic scattering, shown in yellow. Logarithmic scale was used on the y-axis.

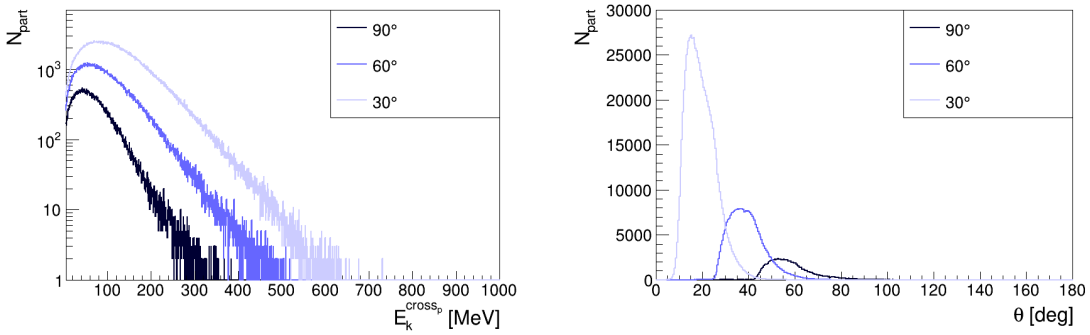

Figure 3.23: Kinetic energy (left) and polar angle (right) distributions of protons at the air-MULTIPASS crossing in the three angular configurations in carbon simulations. The increase in the flux of particles entering the detector as the positioning angle decreases is observed here, unlike in the case of proton simulations. Logarithmic scale was used on the y-axis for the energy histogram.

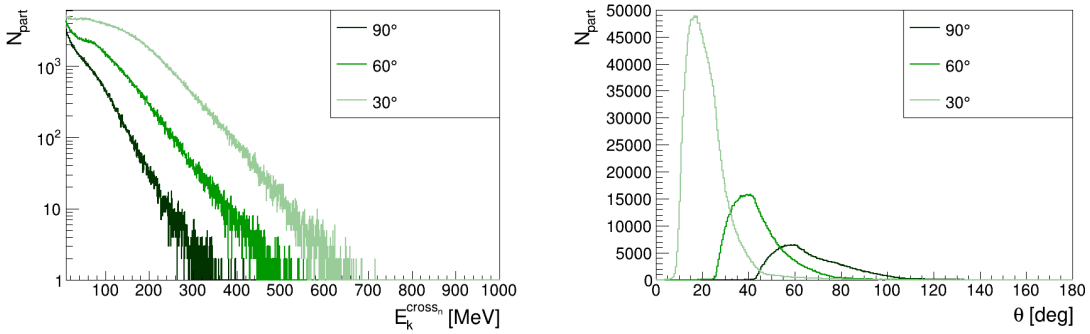

Figure 3.24: Kinetic energy (left) and polar angle (right) distributions of neutrons at the air-MULTIPASS crossing in the three angular configurations in carbon simulations. Logarithmic scale was used on the y-axis for the energy histogram.

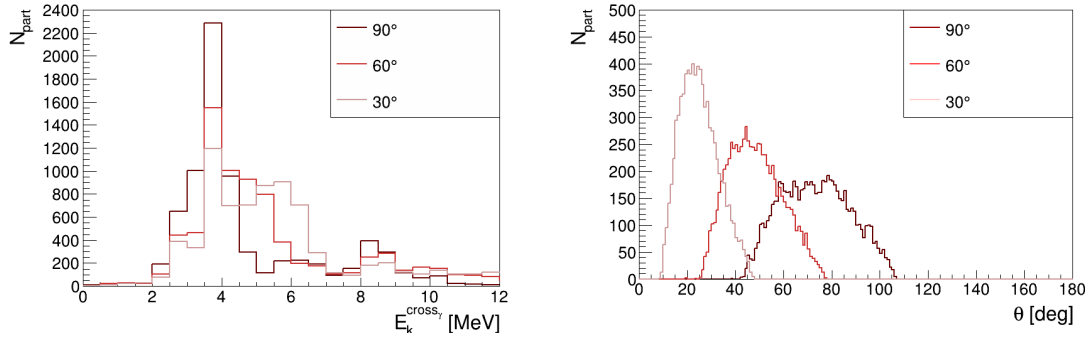

Figure 3.25: Kinetic energy (left) and polar angle (right) distributions of photons at the air-MULTIPASS crossing in the three angular configurations in carbon simulations.

	30° $[\#i/n_{prim}]$	60° $[\#i/n_{prim}]$	90° $[\#i/n_{prim}]$
p ($E_k^{\text{cross}_p} > 5\text{MeV}$)	$1.657 \cdot 10^{-2}$	$6.052 \cdot 10^{-3}$	$1.870 \cdot 10^{-3}$
n ($E_k^{\text{cross}_n} > 10\text{MeV}$)	$3.258 \cdot 10^{-2}$	$1.235 \cdot 10^{-2}$	$5.354 \cdot 10^{-3}$
γ	$1.505 \cdot 10^{-4}$	$1.521 \cdot 10^{-4}$	$1.493 \cdot 10^{-4}$

Table 3.4: Flux of protons, neutrons, and photons at the at the air-MULTIPASS crossing in carbon simulations. The number of simulated primaries is $5 \cdot 10^7$.

able also at 30°. Indeed, in this case, protons resulting from projectile fragmentation are not absorbed by the target, ensuring an acceptable statistics even at lower angles. Thus, the same trend observed for neutrons in Figure 3.13 in the proton simulations is also evident for protons: an increase in the number of incoming particles as the angle relative to the beam propagation direction decreases.

3.3 Study of Clinical Patients

In order to evaluate the performance of MULTIPASS in a clinical context, two simulations of actual treatment plans were carried out using data from the CNAO database. Two patients have been simulated: PZ0, treated with proton beams, and PZ6, treated with carbon ions. Both were suffered from head and neck district tumors, conditions whose progression could lead to the filling or emptying of anatomical cavities, due to variations in tumor configuration, thus making adequate range monitoring necessary. Moreover, the significant size of the tumor mass and its superficial location result in the emission of numerous secondary particles following irradiation. Therefore, this situation proves to be functional for the characterization of the electronics read-out conditions of the MULTIPASS detector.

In these simulations, a trigger option was built to reduce the size of the FLUKA output file: an event is recorded if it generates at least one energy release within the detector. This approach makes the framework more realistic for a real treatment plan, since triggers are typically employed in the electronic registration of events used for range monitoring. This is particularly important given the high number of primary particles simulated and the considerable extent of the tumor target.

In order to simulate the CNAO patients' treatments, the beam nozzle, the table on which the patient is positioned and, possibly, the range shifter were included in the geometrical setup, as shown in Figures 3.26 and 3.32. The range shifter is

a device capable of attenuating the energy of the primary beam and is manually placed between the patient and the beam nozzle. The beam nozzle is a tube where an ultra-high vacuum environment is created to allow the accelerated beam to pass through. The purpose is to minimize friction between the beam particles and air molecules, preventing quality degradation or unwanted deviations. All specific information about the treatment plan, such as the energy, direction of origin and number of the beam particles used, is contained in specific files that are included in the simulation input, so that FLUKA can read them appropriately. The patient's CT (Computerized Tomography) scan was placed within the simulated geometry exactly as the patient would be positioned in the treatment room. Tissue densities are computed from the CT scan thanks to the stochiometric calibration included in the FLUKA software. For each patient, anonymized, the following information is provided: the type of tumor; DICOM (Digital Imaging and COmmunications in Medicine) images of the preparation CT scan; the number, type, and energy of the particle beams used for therapy; the total planned dose and the number of fractions into which the treatment is divided; the possible presence of a range shifter.

Starting from the patient's simulation, the file describing the system geometry was revised to include the MULTIPASS detector (40 planes, each consisting of two layers of 200 fibers aligned along the x and y directions, separated by a mylar thickness) appropriately positioned within the simulated environment. A study was conducted to determine the z production coordinate of secondary particles generated during the treatment, in order to properly position the detector with respect to the tumor location. This aims to maximize the number of particles entering the device, minimizing re-absorption effects due to the long distances particles have to travel before reaching it.

In these simulations, only histograms and particle fluxes ($\Phi_{air-det}$), as defined in Equations 3.2) at the air-detector crossing were extracted. Indeed, the CT geometry is very complex and treats each individual voxel (the fundamental unit of CT volumetric graphics) as a distinct entity. As a result, determining the voxel-particle correlation is quite complex and beyond the scope of this thesis.

3.3.1 Patient PZ0 Treated with Protons

Patient PZ0 was affected by Squamous Cell Carcinoma (SCC). The goal was to deliver a total dose of approximately 60−66 GyE over 33 fractions. It involved the use of three irradiation fields: B1 at 270°, from above the patient's head, B2 at 0°, from the left of the patient, and B3 at 180°, from the right of the patient. Of the three, only B1, which comes from the negative direction of the z-axis, was simulated, spacing an energy range of $66.3 \div 167.7$ MeV and a total of $2.13 \cdot 10^{10}$ protons. The CT scan has thus been positioned respectively. In this case, a range shifter with a thickness of 3 cm was used, centered in z at -16.8 cm, as foreseen by the TPS (Treatment Planning System). The simulation setup is showed in Figure 3.26.

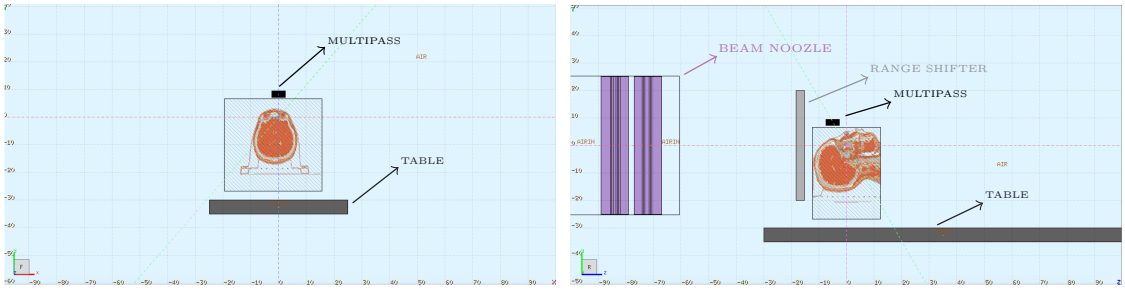

Figure 3.26: Flair transverse and sagittal views of the clinical setup for the patient treated with protons.

Figure 3.27 shows that the z coordinate of the production of the secondary particles coming from the CT (blue for protons, green for neutrons and red for photons) ranges from -10 cm to -2 cm. Consequently, the MULTIPASS detector was placed with the center at -5 cm along the z-axis. An additional peak occurs between -16 cm and -18 cm along z. This is due to the presence of the range shifter, which can cause additional secondary particles production from the primary beam. Indeed, note that the position of the peak coincides with that of the range shifter. In the following analysis, secondary particles produced by the range shifter have been excluded, as the focus is solely on those generated within the patient's body. From a practical standpoint, this means that during the actual treatment, it will be necessary to properly shield particles entering MULTIPASS from the left, a large portion of which originate from the range shifter.

Furthermore, the detector was positioned as close as possible to the patient's head ($\sim$ cm), again to maximize the flux of incoming secondary particles. The

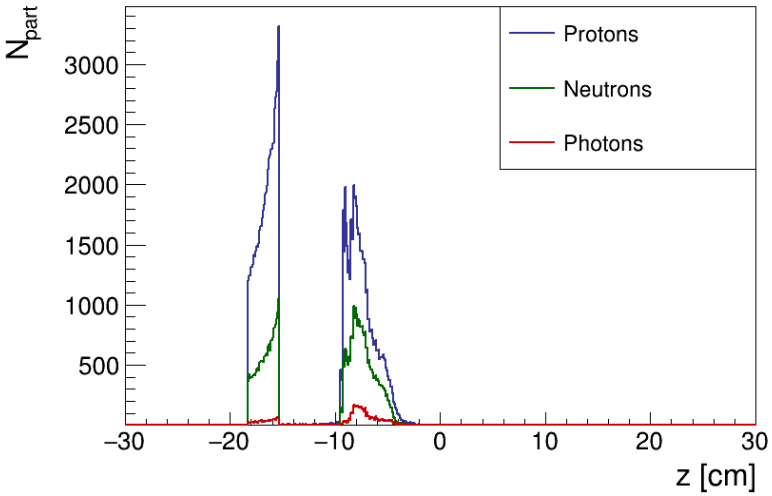

Figure 3.27: z production coordinate of protons, neutrons, and photons resulting from the primary beam interactions with PZ0's body. Note the production between -10 cm and -2 cm relative to the CT, while particles generated from -18 cm to -15 cm are relative to the range shifter.

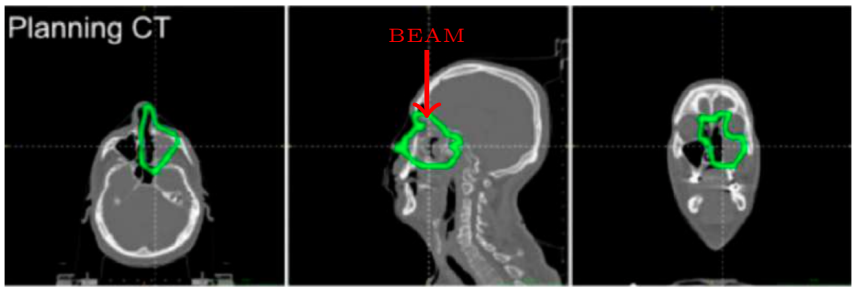

Figure 3.28: Transverse, sagittal, and coronal views of the CT scan of PZ0. The region where the tumor lesion extends is highlighted in green. In the sagittal view, the beam incidence direction is shown with a red arrow.

tumor's ROI (Region Of Interest), shown in Figure 3.28, confirms this choice, as the tumor (green region) predominantly extends into the superficial region of the face.

Figures 3.29, 3.30, and 3.31 show the kinetic energy and polar angle distributions obtained for the simulation of the treatment plan of PZ0 with protons, while Table 3.5 contains the flux of particles at the air-detector crossing.

In the analysis, only particles entering in MULTIPASS with a polar angle greater than 45° were considered, in order to eliminate, as mentioned above, the contribution of secondary particles generated by the range shifter. With respect to the results obtained from the proton simulations using the PMMA target (see Section 3.2.1),

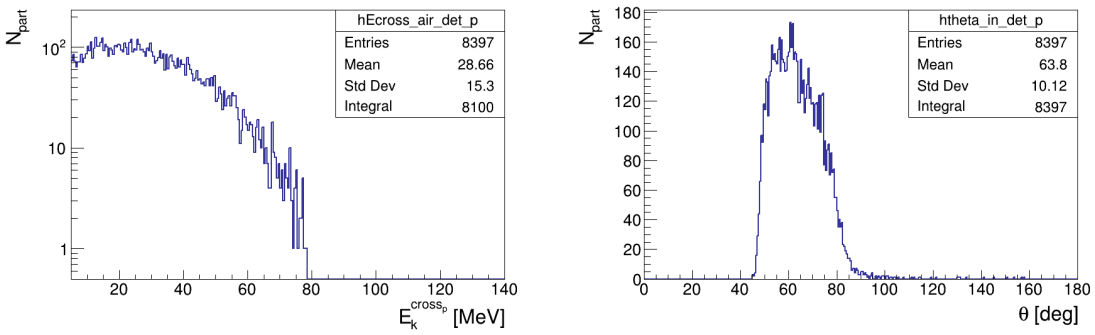

Figure 3.29: Kinetic energy (left) and polar angle distributions (right) of protons at the air-MULTIPASS detector in the treatment with protons of PZ0.

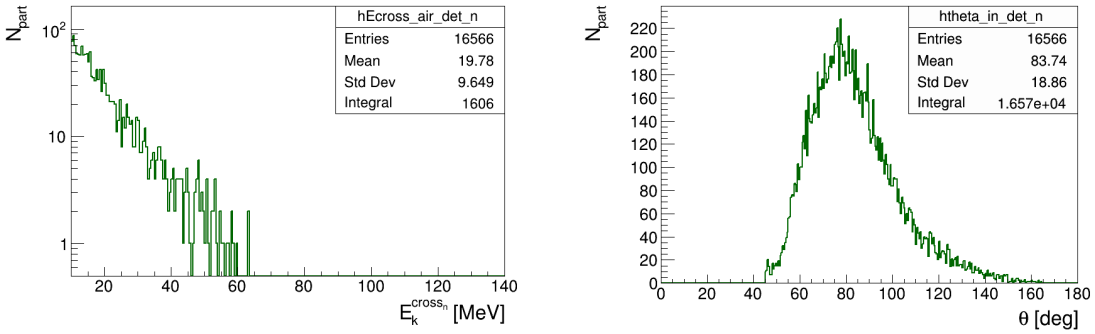

Figure 3.30: Kinetic energy (left) and polar angle distributions (right) of neutrons at the air-MULTIPASS detector in the treatment with protons of PZ0.

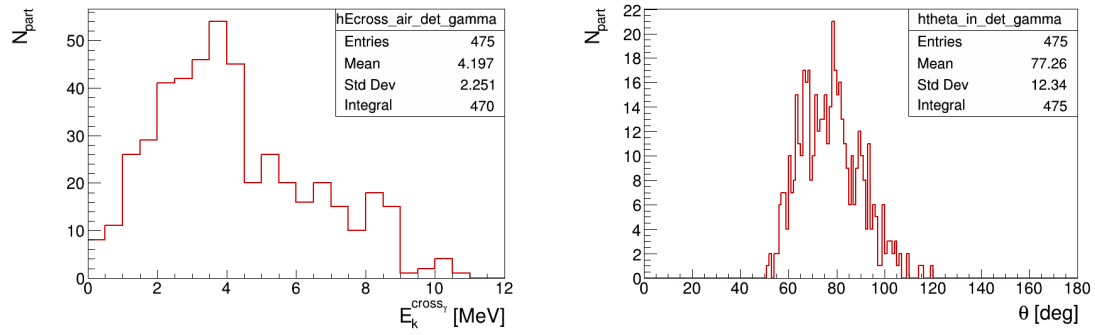

Figure 3.31: Kinetic energy (left) and polar angle distributions (right) of photons at the air-MULTIPASS detector in the treatment with protons of PZ0.

p ($E_k^{\text{cross}_p} > 5\text{MeV}$) $[\#p/n_{prim}]$	n ($E_k^{\text{cross}_n} > 10\text{MeV}$) $[\#n/n_{prim}]$	γ $[\#\gamma/n_{prim}]$
$3.803 \cdot 10^{-7}$	$7.540 \cdot 10^{-8}$	$2.207 \cdot 10^{-8}$

Table 3.5: Flux of protons, neutrons, and photons at the air-MULTIPASS crossing in the simulation of PZ0 treated with protons. The number of simulated primaries is $2.13 \cdot 10^{10}$.

the incoming particle fluxes are lower for all three types of particles analyzed. It is worth noting that, despite the higher average energy of the primary beam and the larger number of particles used, by a factor of $4 \cdot 10^2$, with respect to the study with the PMMA target, the number of secondaries reaching the detector is actually lower, as observed from the comparison between Table 3.2 and Table 3.5. This happens because, unlike in the PMMA case, secondaries must pass through a considerable nonuniform thickness of material to exit the patient's body, leading to a significant re-absorption of many particles before they can reach the detector. Furthermore, since the energies involved are higher, the elastic scattering interactions which lead to the emission of protons and neutrons will be more frequent and more pronounced, reducing the incoming flux to the detector.

Another significant difference is the higher number of protons compared to neutrons, unlike the study reported in Section 3.2.1. By focusing on Figure 3.30, it becomes clear that there is a significant discrepancy between the total number of neutrons at the air-detector crossing and the number of neutrons above threshold. This suggests that the majority of neutrons generated during the treatment which enter the detector are low-energy, with only a small fraction surviving the 10 MeV energy cut-off.

3.3.2 Patient PZ6 Treated with ^{12}C

Patient PZ6 was affected by ITAC (Intestinal Type Adeno Carcinoma). The patient was treated with carbon ions, delivering a dose of 65.5 GyE over a total of 16 fractions. The therapy involved the use of two irradiation fields, B1 at 15°, from the left of the patient, and B3 at 270°, from above the patient's head. In this work, only B3, made of a total $5.98 \cdot 10^8$ carbon ions and spanning an energy range of $164.4 \div 301.4$ MeV/u, was simulated. As in the previous case, the patient's CT has been positioned accordingly. Furthermore, the range shifter was not employed (in

the geometry view, depicted in Figure 3.32, it is present, but it is filled with air).

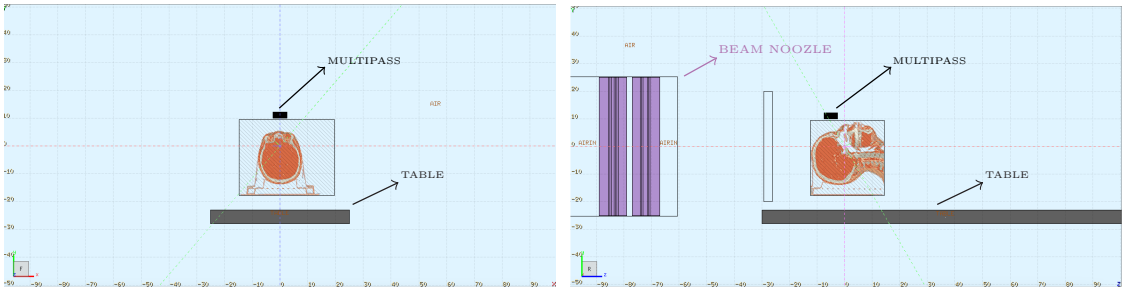

Figure 3.32: Flair transverse and sagittal views of the clinical setup for the patient treated with ^{12}C ions.

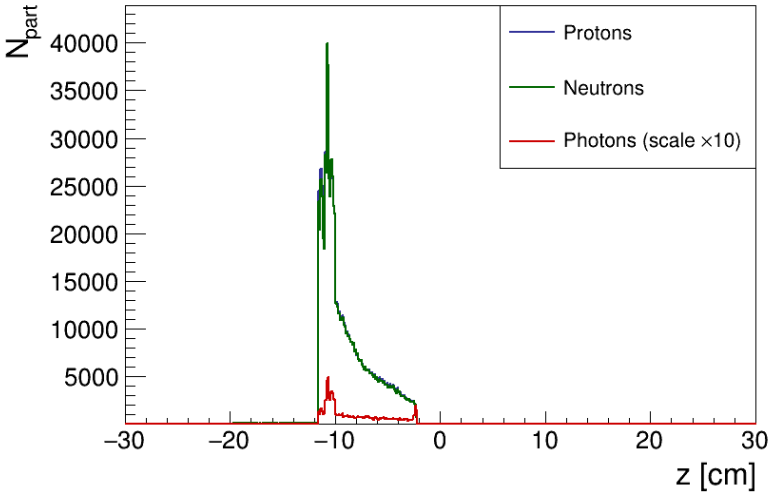

Figure 3.33: z production coordinates of protons, neutrons, and photons resulting from the primary beam interactions with PZ6's body. Note the production peak between -12 cm and -10 cm, which corresponds to the Bragg peak. Photon distribution is scaled by a factor 10 to ensure better readability.

Figure 3.33 present the histograms obtained in the preliminary study related to the production position of protons (blue), neutrons (green) and photons (red). For all three particle species, the production occurs between -12 cm and -2 cm. Consequently, the detector was again positioned with the center at -5 cm along the z-axis. Similarly to the previous case, analyzed in Section 3.3.1, since the tumor extends into the sinonasal area, the detector was positioned as close as possible to the patient's face ($\sim$ 1 cm), to maximize the incoming secondary fluxes.

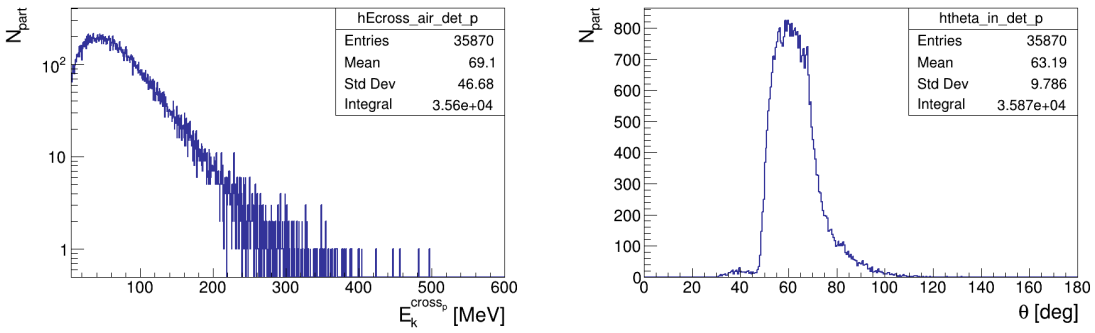

Figure 3.34: Kinetic energy (left) and polar angle (right) distributions of protons at the the air-MULTIPASS crossing in the treatment with carbon ions of PZ6.

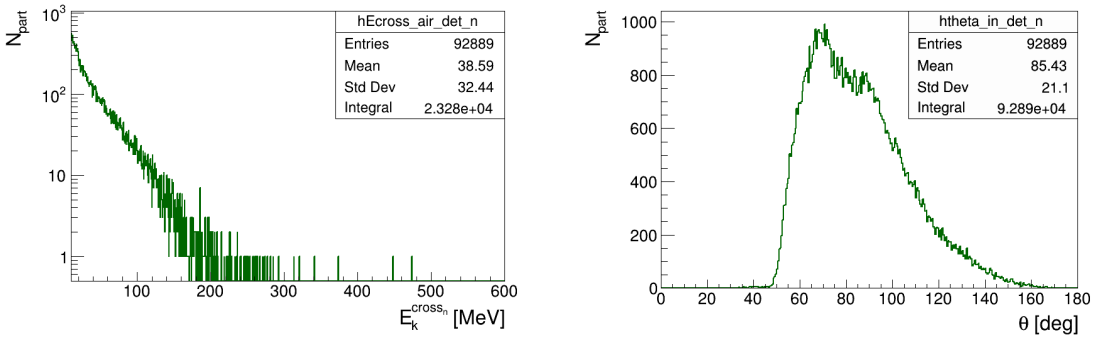

Figure 3.35: Kinetic energy (left) and polar angle (right) distributions of neutrons at the the air-MULTIPASS crossing in the treatment with carbon ions of PZ6.

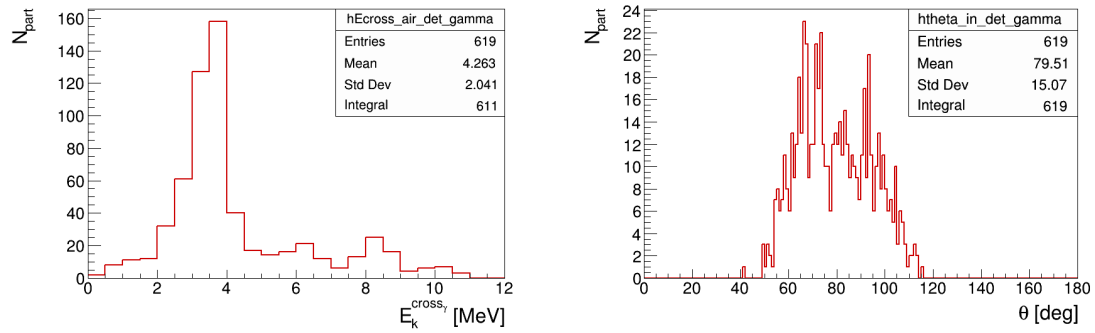

Figure 3.36: Kinetic energy (left) and polar angle (right) distributions of photons at the the air-MULTIPASS crossing in the treatment with carbon ions of PZ6.

In Figures 3.34, 3.35 and 3.36 are depicted the kinetic energy and polar angle distributions obtained for the simulation of the treatment plan of PZ6 with carbon ions for protons, neutrons and photons, while Table 3.6 presents the flux of particles at the air-detector crossing.

p ($E_k^{\mathrm{cross}_p} > 5\mathrm{MeV}$) $[\#p/n_{prim}]$	n ($E_k^{\mathrm{cross}_n} > 10\mathrm{MeV}$) $[\#n/n_{prim}]$	γ $[\#\gamma/n_{prim}]$
$5.953 \cdot 10^{-5}$	$3.893 \cdot 10^{-5}$	$1.022 \cdot 10^{-6}$

Table 3.6: Flux of protons, neutrons, and photons at the air-MULTIPASS crossing in the simulation of PZ6 treated with carbon ions. The number of simulated primaries is $5.98 \cdot 10^8$.

Going over the results obtained from the study with the PMMA target, the incoming data for protons and neutrons are of the order of 10^4. Protons predominantly originate from projectile fragmentation, as the angular distribution remains sharply peaked around 60°, suggesting a preferred emission direction. On the other hand, neutrons mainly arise from scattering interactions. The width of the angular distribution shows how, as a result of scatterings which alter their direction of motion, they enter MULTIPASS with multiple angles.

In the case of carbon treatments, even in a more complex real scenario, MULTIPASS is able to detect a sufficiently high number of secondary particles. However, as mentioned in Section 3.3.1, the statistics are reduced compared to those analyzed in Section 3.2.2 due to the absorption effect caused by the CT geometry.

Conclusions

This thesis work is part of the PRIN (Progetti di Rilevante Interesse Nazionale) MULTIPASS (MULTIPle trAcker for Secondary particleS monitoring) project, which aims to develop the prototype of a scintillating fiber detector to track various types of secondary particles produced in hadrontherapy treatments for range monitoring purposes. A key aspect of the project is the design of the read-out electronics, based on SPAD (Single Photon Avalanche Diodes) matrices, developed in collaboration with Centro Ricerche "Enrico Fermi" (CREF, Roma) and Fondazione Bruno Kessler (FBK, Trento). To understand the required performance of the read-out system, this thesis project conducted a preliminary study on the secondary particle fluxes, particularly of protons, neutrons, and photons (p, n, γ), expected to enter the detector in different possible scenarios.

In the first part of the study, simulations were performed using a simplified geometry, including a radiological tissue equivalent target, made of PMMA (polymethylmethacrylate), irradiated by a single monoenergetic pencil beam of protons, with an energy of 112.3 MeV, and carbon ions, with an energy of 220 MeV/u. In both cases, the beam consisted of $5 \cdot 10^7$ particles. The Bragg peak of the beams was positioned at the same depth of $\sim$8 cm within the PMMA target. The angular positioning of the detector was varied in the study, at 30°, 60° and 90° with respect to the beam incoming direction. Indeed, the objectives of this study, performed in an elementary geometrical configuration, are analyzing the number of secondary particles generated by a single pencil beam and providing a comprehensive analysis of secondary particle fluxes at the entrance of MULTIPASS, which are, mainly in the case of secondary protons and neutrons, angle-dependent.

Proton simulations showed that the maximum incoming particle flux per primary particle is expected with the detector positioned at 60° for protons, $7.368 \cdot 10^{-5}$ $\#p$/primary, at 30° for neutrons, $1.051 \cdot 10^{-3}$ $\#n$/primary, and at 90° for prompt

photons, $2.910 \cdot 10^{-5}$ $\#\gamma$/primary. Instead, in the case of simulations with carbon ions, the maximum secondary incoming fluxes per primary particle are reached at 30° for both protons and neutrons, $1.657 \cdot 10^{-2}$ $\#p$/primary and $3.258 \cdot 10^{-2}$ $\#n$/primary, and at 60° for prompt photons, $1.521 \cdot 10^{-4}$ $\#\gamma$/primary.

In the second part of the study, since MULTIPASS ultimately aims to design a detector for range monitoring in hadrontherapy treatments both with proton and carbon ion beams, simulations were performed using the treatment plans of two patients treated at the CNAO (Centro Nazionale di Adroterapia Oncologica) therapy center, during a clinical trial. One patient was treated with protons, with kinetic energy ranging from 66.3 MeV to 167.7 MeV, and a total particle beam statistics of $2.13 \cdot 10^{10}$; the other was treated with carbon ions, with kinetic energy ranging from 164.4 MeV/u to 301.4 MeV/u, and a total particle beam statistics of $5.98 \cdot 10^{8}$. The aim of this second part of the work was to better understand the secondary particle fluxes that might actually be expected at the detector entrance in a real clinical scenario. Both the patients' CT scans and the irradiation fields, specified in their respective treatment plans, were included in the simulations. The MULTIPASS detector was positioned close to the patient, to maximize the statistics of incoming secondaries.

In general, the expected fluxes were observed to be lower compared to those obtained in the simplified geometry using the PMMA volume. In the case of the patient treated with protons, the fluxes per primary particle expected at the detector entrance correspond to $3.803 \cdot 10^{-7}$ $\#p$/primary, $7.540 \cdot 10^{-8}$ $\#n$/primary and $2.207 \cdot 10^{-8}$ $\#\gamma$/primary, reduced by a factor of $\sim 1.9 \cdot 10^{2}$, $\sim 1.4 \cdot 10^{4}$ and $\sim 1.3 \cdot 10^{3}$ respectively, compared to the geometry with the PMMA target. For the patient treated with carbon ions, they are $5.953 \cdot 10^{-5}$ $\#p$/primary, $3.893 \cdot 10^{-5}$ $\#n$/primary and $1.022 \cdot 10^{-6}$ $\#\gamma$/primary, reduced by a factor of $\sim 2.8 \cdot 10^{2}$, $\sim 8.4 \cdot 10^{2}$ and $\sim 1.5 \cdot 10^{2}$ respectively, compared to the geometry with the PMMA target. This effect aligns with expectations, as the thickness that secondary particles must traverse in the CT geometry is grater than in the case of the simple configuration with the PMMA target. As a result, a considerable fraction of the produced particles is absorbed and goes undetected. Further studies of treatment plans, including larger tumors, close to the patient's surface, with higher primary irradiating particle statistics, may be necessary to determine whether the detector

will need to operate at higher detection performance.

In conclusion, the results obtained during this proof of principle, based on a study employing Monte Carlo simulations, are of great importance, as they will guide the development of an innovative read-out electronics system, with the MULTIPASS detector serving as a functioning prototype. This system could be utilized in the future to develop efficient detectors for range monitoring in hadrontherapy, with the potential feasibility of such devices paving the way for more effective cancer treatments.

Bibliography

[1] World Health Organization, Cancer, 2020. [Online]. Available: https://www.who.int/news-room/fact-sheets/detail/cancer.

[2] National Cancer Institute, What Is Cancer? Accessed: September 17, 2007, 2007. [Online]. Available: https://www.cancer.gov/about-cancer/understanding/what-is-cancer.

[3] "I numeri del cancro in italia 2023," AIRTUM - Associazione Italiana Registri Tumori, Tech. Rep., 2023. [Online]. Available: https://www.registri-tumori.it/cms/pubblicazioni/i-numeri-del-cancro-italia-2023.

[4] World Health Organization, Cancer Fact Sheets, Accessed: 2024-10-05, 2023. [Online]. Available: https://www.who.int/news-room/fact-sheets/detail/cancer.

[5] N. J. Carron, An Introduction to the Passage of Energetic Particles through Matter. Boca Raton, FL: CRC Press, 2006.

[6] A. E. Nahum, J. Seuntjens, F. H. Attix, P. Andreo, and D. T. Burns, Fundamentals of Ionizing Radiation Dosimetry. Hoboken, NJ: Wiley, 2017.

[7] W. R. Leo, Techniques for Nuclear and Particle Physics Experiments. Berlin, Heidelberg: Springer-Verlag Berlin Heidelberg GmbH, 1994.

[8] K. Nakamura and (. D. Group), "Review of Particle Physics," *Journal of Physics G: Nuclear and Particle Physics*, vol. 37, no. 7A, Jul. 2010. DOI: 10.1088/0954-3899/37/7A/075021.

[9] R. Hazem, "Interaction of Proton Beam with Human Tissues in Proton Therapy," in *Proton Therapy*, T. J. FitzGerald, Ed., Rijeka: IntechOpen, 2023, ch. 5. DOI: 10.5772/intechopen.1003186.

[10] M. Testa, "Charged particle therapy, ion range verification, prompt radiation," Theses, Université Claude Bernard - Lyon I, Oct. 2010.

[11] V. L. Highland, "Some Practical Remarks on Multiple Scattering," *Nucl. Instrum. Meth.*, vol. 129, p. 497, 1975. DOI: 10.1016/0029-554X(75)90743-0.

[12] H. A. Bethe, "Molière's Theory of Multiple Scattering," *Phys. Rev.*, vol. 89, pp. 1256–1266, 6 Mar. 1953. DOI: 10.1103/PhysRev.89.1256.

[13] K. Gunzert, H. Iwase, D. Schardt, and R. Simon, "Secondary beam fragments produced by 200 MeV u^{-1} 12C ions in water and their dose contributions in carbon ion radiotherapy," *New Journal of Physics - NEW J PHYS*, vol. 10, Jul. 2008. DOI: 10.1088/1367-2630/10/7/075003.

[14] M. Joiner and A. V. Kogel, Basic Clinical Radiobiology. CRC Press, 2018.

[15] A. Nakata, K. Ariyoshi, Y. Abe, *et al.*, "Cytogenetic Biodosimetry in Radiation Emergency Medicine: 3. The Basics of Chromosomes for Biodosimetry," pp. 82–90, May 2022. DOI: 10.51083/radiatenvironmed.11.2_82.

[16] M. Durante and H. Paganetti, "Nuclear physics in particle therapy: A review," *Reports on Progress in Physics*, vol. 79, p. 096 702, Aug. 2016. DOI: 10.1088/0034-4885/79/9/096702.

[17] S. Deycmar, E. Faccin, T. Kazimova, *et al.*, "The relative biological effectiveness of proton irradiation in dependence of dna damage repair," *The British Journal of Radiology*, vol. 93, p. 20 190 494, Nov. 2019. DOI: 10.1259/bjr.20190494.

[18] J. Chavaudra and A. Bridier, "Definition of volumes in external radiotherapy: ICRU reports 50 and 62," *Cancer Radiothérapie: Journal de la Société Française de Radiothérapie Oncologique*, vol. 5, no. 5, pp. 472–478, 2001. DOI: 10.1016/s1278-3218(01)00117-2.

[19] H. Paganetti, "Range uncertainties in proton therapy and the role of Monte Carlo simulations," *Physics in Medicine and Biology*, vol. 57, no. 11, R99–R117, 2012. DOI: 10.1088/0031-9155/57/11/R99.

[20] S. Muraro, G. Battistoni, F. Collamati, *et al.*, "Monitoring of Hadrontherapy Treatments by Means of Charged Particle Detection," *Frontiers in Oncology*, vol. 6, p. 177, Aug. 2016. DOI: 10.3389/fonc.2016.00177.

[21] J. Krimmer, D. Dauvergne, J. Létang, and E. Testa, "Prompt-gamma monitoring in hadrontherapy: A review," *Nuclear Instruments and Methods in Physics Research Section A: Accelerators, Spectrometers, Detectors and Associated Equipment*, vol. 878, pp. 58–73, Jan. 2018. DOI: 10.1016/j.nima.2017.07.063.

[22] K. Parodi, "PET monitoring of hadrontherapy," *Nuclear Medicine Review*, vol. 15, no. C, pp. 37–42, 2012.

[23] J. Lerendegui-Marco, J. Balibrea-Correa, V. Babiano, L. Caballero, C. Domingo-Pardo, and I. Ladarescu, "Simultaneous neutron and gamma imaging system for real time range and dose monitoring in Hadron Therapy and nuclear security applications," *EPJ Web of Conferences*, vol. 261, p. 05 001, Jan. 2022. DOI: 10.1051/epjconf/202226105001.

[24] J. Mattingly, K. S. Ytre-Hauge, and K. Skjerdal, "A Monte Carlo Feasibility Study for Neutron-Based Real-Time Range Verification in Proton Therapy," *Scientific Reports*, vol. 9, p. 2011, 2019. DOI: 10.1038/s41598-019-38611-w.

[25] T. Nishio, A. Miyatake, K. Inoue, *et al.*, "Experimental verification of proton beam monitoring in a human body by use of activity image of positron-emitting nuclei generated by nuclear fragmentation reaction," *Radiological physics and technology*, vol. 1, pp. 44–54, Nov. 2008. DOI: 10.1007/s12194-007-0008-8.

[26] W. C. Hsi, D. J. Indelicato, C. E. Vargas, S. Duvvuri, Z. Li, and J. R. Palta, "In vivo verification of proton beam path by using post-treatment PET/CT imaging.," *Medical physics*, vol. 36 9, pp. 4136–46, 2009. DOI: 10.1118/1.3193677.

[27] X. Zhu, S. España, J. Daartz, *et al.*, "Monitoring proton radiation therapy with in-room PET imaging," *Physics in medicine and biology*, vol. 56, pp. 4041–57, Jul. 2011. DOI: 10.1088/0031-9155/56/13/019.

[28] I. Mattei *et al.*, "Prompt-γ production of 220 MeV/u (12)C ions interacting with a PMMA target," *JINST*, vol. 10, no. 10, P10034, 2015. DOI: 10.1088/1748-0221/10/10/P10034.

[29] C. Agodi, F. Bellini, P. Cirrone, *et al.*, "Precise measurement of prompt photon emission from 80 MeV/u carbon ion beam irradiation (vol 7, p03001, 2012)," *JOURNAL OF INSTRUMENTATION*, vol. 7, Mar. 2012. DOI: 10.1088/1748-0221/7/03/P03001.

[30] H. Seo, S. Lee, H. Jeong, *et al.*, "AID – A Novel Method for Improving the Imaging Resolution of a Table-Top Compton Camera," *Nuclear Science, IEEE Transactions on*, vol. 55, pp. 2527–2530, Nov. 2008. DOI: 10.1109/TNS.2008.2000777.

[31] Thirolf, P.G., Aldawood, S., Böhmer, M., *et al.*, "A Compton Camera prototype for prompt gamma medical imaging," *EPJ Web of Conferences*, vol. 117, p. 05 005, 2016. DOI: 10.1051/epjconf/201611705005.

[32] E. Haettner, H. Iwase, and D. Schardt, "Experimental fragmentation studies with 12C therapy beams," *Radiation Protection Dosimetry*, vol. 122, no. 1-4, pp. 485–487, Dec. 2006, ISSN: 0144-8420. DOI: 10.1093/rpd/ncl402.

[33] L. Piersanti, F. Bellini, F. Bini, *et al.*, "Measurement of charged particle yields from PMMA irradiated by a 220 MeV/u 12C beam," *Physics in Medicine Biology*, vol. 59, no. 7, p. 1857, Mar. 2014. DOI: 10.1088/0031-9155/59/7/1857.

[34] G. Traini, I. Mattei, G. Battistoni, *et al.*, "Review and performance of the Dose Profiler, a particle therapy treatments online monitor," *Physica Medica*, vol. 65, pp. 84–93, Sep. 2019. DOI: 10.1016/j.ejmp.2019.07.010.

[35] M. Fischetti, G. Baroni, G. Battistoni, *et al.*, "Inter-fractional monitoring of C ions treatments: Results from a clinical trial at the CNAO facility," *Scientific Reports*, vol. 10, no. 1, p. 20 735, 2020. DOI: 10.1038/s41598-020-77843-z.

[36] M. Toppi, I. Avanzolini, L. Balconi, *et al.*, "PAPRICA: The Pair Production Imaging Chamber—Proof of Principle," *Frontiers in Physics*, vol. 9, p. 568 139, Mar. 2021. DOI: 10.3389/fphy.2021.568139.

[37] D. J. Thompson and A. A. Moiseev, "Pair production detectors for Gamma-ray astrophysics," *Gamma-ray Astrophysics*, 2020.

[38] S. Valle, G. Battistoni, V. Patera, *et al.*, "The MONDO project: A secondary neutron tracker detector for particle therapy," *Nuclear Instruments and Methods in Physics Research Section A: Accelerators, Spectrometers, Detectors and Associated Equipment*, vol. 845, pp. 556–559, 2017, Proceedings of the Vienna Conference on Instrumentation 2016, ISSN: 0168-9002. DOI: 10.1016/j.nima.2016.05.001.

[39] M. Marafini, L. Gasparini, R. Mirabelli, *et al.*, "MONDO: A neutron tracker for particle therapy secondary emission characterisation," *Physics in Medicine and Biology*, vol. 62, pp. 3299–3312, Mar. 2017. DOI: 10.1088/1361-6560/aa623a.

[40] C. Ahdida, D. Bozzato, D. Calzolari, *et al.*, "New Capabilities of the FLUKA Multi-Purpose Code," *Frontiers in Physics*, vol. 9, p. 788 253, 2022. DOI: 10.3389/fphy.2021.788253.

[41] G. Battistoni, T. Boehlen, F. Cerutti, *et al.*, "Overview of the FLUKA code," *Annals of Nuclear Energy*, vol. 82, pp. 10–18, 2015. DOI: 10.1016/j.anucene.2014.11.007.

[42] V. Vlachoudis, "FLAIR: A Powerful But User Friendly Graphical Interface For FLUKA," in *Proc. Int. Conf. on Mathematics, Computational Methods & Reactor Physics (M&C 2009)*, Saratoga Springs, New York, 2009.